DISCLAIMER

Federal Agency and Organization Element to Which Report is Submitted:
Department of Energy (DOE)
National Energy Tech Lab
Attn: Matthew Adams, Program Manager

DOE Contract Number: DE-FE0031617

Project Title: Novel Modular Heat Engines with sCO_2 Bottoming Cycle Utilizing Advanced Oil-Free Turbomachinery

Principal Investigator (PI):
Dr. Bugra Ertas
Chief Engineer
GE Aerospace Research, K1-2C-34A,
1 Research Circle, Niskayuna, NY 12309
Phone: 518-779-0930
Email: ertas@geaerospace.com

Submission Date: 02/09/2026

Recipient Organization:
Matthew Adams
Federal Project Manager
Advanced Energy Systems Team
U.S. DOE National Energy Technology Laboratory
3610 Collins Ferry Road
Morgantown, WV 26507-0880
Phone: 304-285-1321
Email: Matthew.F.Adams@netl.doe.gov

Performance Period: May 2020- June 2025

Report Type: Final Report

Signature of PI:
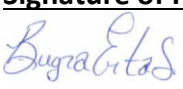
Bugra Ertas

DISCLAIMER

ACKNOWLEDGEMENT

This material is based upon work supported by the Department of Energy under Award Number DE-FE0031617.

TABLE OF CONTENTS

EXECUTIVE SUMMARY

The following report summarizes the entirety of the work performed for project DE-FE0031617. The report outlines the engineering, design, procurement, fabrication, and partial installation of the test system. The project was not fully completed as assembly and testing of the rotating system was not achieved due to time and budget constraints. To date all hardware has been fabricated in addition to major component procured ready for final assembly and testing. The report also outlines remaining costs elements that are required to fully achieve initial project objectives. The project output three ASME Turboexpo Conference papers focused on the design and analysis of the test system.

This report presents the thermal, mechanical, and electric machine design of a 27krpm rotating test rig aimed at reducing technical risks with hermetic oil-free super-critical carbon dioxide (sCO_2) turbomachinery. The test rig rotor system is based on a conceptual turbomachine design discussed that evaluates a sCO_2 waste heat recovery (WHR) unit for land-based gas turbines at natural gas (NG) compressor stations. The key novelty of the hermetic sCO_2 turbomachine concept is the utilization of additively manufactured CO_2 gas bearings and a CO_2-immersed direct-drive permanent magnet (PM) electric machine. The previous effort on conceptual design identified 3 main technical risks, which included thrust bearing load capacity, rotordynamics, and thermal performance of the system. Therefore, key requirements of the test vehicle include the ability to test the rotor system in a 400psi (27.6 bar) hermetic CO_2 operating environment, apply up to 1,500 lbs (6.7 kN) of rotor thrust loads, capability to assess rotordynamics with radial gas bearings, inclusion of instrumentation to assess thrust bearing load capability, and flexibility for varying secondary cooling flows to confirm thermal model predictions. Design topics such as rotordynamics, bearing design, and electric machine design are addressed, while highlighting critical elements. In addition, additive build trials for Inconel 718 radial and thrust bearings were performed to prove the manufacturability of the bearing design concepts. The results of the design efforts yield a test rig concept with ability to operate at 27,000 rpm, apply thrust loads to 1,500 lbs, deliver CO_2 up to 800psi, and modulate cooling flows.

1. INTRODUCTION

Supercritical carbon dioxide power cycles have become an active area of research with interest in applications such as concentrated solar power [1, 2] and waste heat recovery (WHR) [3-5]. Using sCO_2 as the working fluid allows for an efficient, self-contained, and remotely operable solution for a turbine based modular heat engine. This is particularly the case for pipeline natural gas (NG) compressor stations, as the Annual Energy Outlook (AEO) for 2022 forecasts NG to be the most consumed form of energy over the next 30 years [6]. The predicted increase in demand for NG will no doubt require increased pipeline throughput; dictated by compressor station capacity. To help meet these demands, while minimizing emissions, reference paper [7] investigates the implementation of a sCO_2 WHR bottoming cycle powered by the exhaust gas of an industrial 34kHP aeroderivative gas turbine. The bottoming cycle was configured to operate as a recuperated cascaded Brayton cycle operating with 237 bar and 485^o C sCO_2 on the high-pressure side and 83 bar and 35^o C on the low-pressure side, while recovering 8.5MW of emission-free electric power from the gas turbine exhaust. Figure 1 shows a typical compressor station and how a WHR unit could be used to either increase capacity or generate a surplus of 60Hz electrical power, expanding the number of suitable compressor stations for WHR. Although the concept in Figure 1 provides usage mode flexibility, achieving widespread implementation also requires minimizing “price paid for power generated” [8]. Hence, reference [7] proposes a WHR system using a hermetic oil-free sCO_2 dual-spool power train [9] in efforts to lower capital costs and minimize operating expenditures, while eliminating 600-800 metric tons CO_2 leakage annually typically expected from recent 10MW-scale sCO_2 power turbomachinery demonstrators [10-12]. Figure 2b illustrates the dual spool concept. Unlike the conventional approach (Figure 2a) the oil-free hermetic architecture allows for leakage free operation while enabling the removal of high-cost items like the lubrication skid, power transmission gearbox, and dry gas seal systems. The concept uses a high-speed gas-generator aerodynamically coupled to a low-speed power turbine and generator drivetrain. The reference paper’s [7] analysis and sizing study generated a concept layout of the power drivetrains, where Figure 2c shows the cross-section of the high-speed gas generator machine. The machine architecture is comprised of a sCO_2 centrifugal compressor stage mechanically coupled to a three-stage sCO_2 expander, which then couples to a 1MW direct-drive starter-generator. Through this study several technical risks were identified for enabling this architecture, where the first key risk was the implementation of oil-free bearings into high-power turbomachinery.

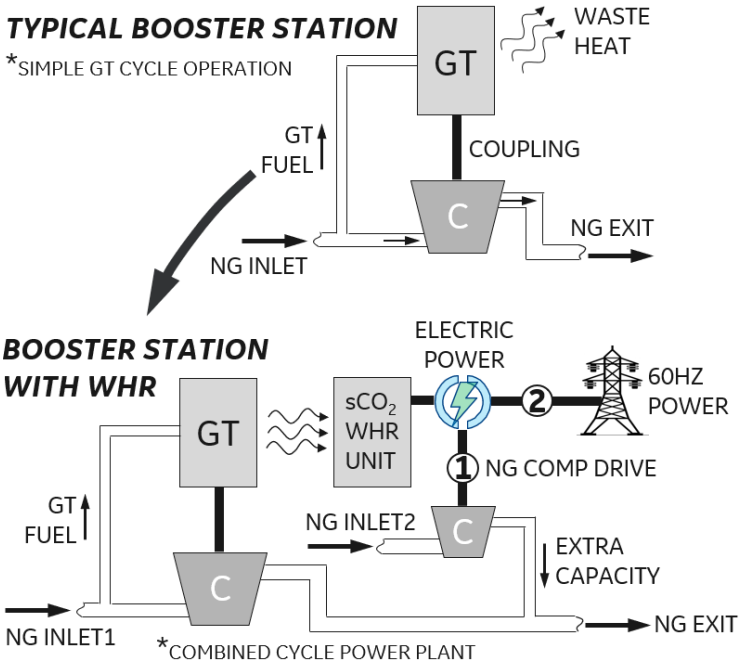

Fig 1. Natural gas booster station with WHR: GT- gas turbine, C- NG compressor

Hermetic turbomachines in the mega-Watt power range are not a new concept, as several past efforts [13-15] have employed a hermetic casing with an oil-free immersed motor-compressor. Mainly used for oil and gas operations, these past case studies utilize magnetic bearings to achieve oil-free rotor operation. Magnetic bearing systems are a matured and industrialized actively controlled bearing technology that enables oil-free operation of high-performance turbomachinery. These bearings also have the advantage of active vibration control and the ability to tune force coefficients for the specific applications. However, magnetic bearings are relatively complex systems with a high cost, have modest temperature limitations, and can sustain a limited number rotor-drops from power interruption before requiring maintenance. To further reduce complexity, cost, and improve overall system reliability, process gas film lubricated bearings were chosen for the conceptual turbomachine design (Figure 2c). Past work by Conboy et al. [16] in 2012 published results from an oil-free hermetic sCO_2 power cycle utilizing 1.5-inch (38mm) diameter radial hydrodynamic gas foil bearings [17] and a 4-inch (102mm) outer diameter hydrodynamic foil thrust bearing [17]. The sCO_2 power system produced 20kWe at a max rotating speed of 52krpm. Although a notable achievement for sCO_2 power systems, scaling foil bearings to larger megawatt rotors has yet to be proven. Unlike the hydrodynamic foil bearing in Conboy's work [16], the current report looks to implement externally pressurized (hybrid) gas bearings integrated with novel hermetic squeeze film dampers (HSFD) in the bearing support. Bearing load capacity and damping limitations with existing gas bearing technology were key considerations to the development of hybrid gas bearings with HSFD [18-22]. Although numerous benchtop and component tests have been conducted on these bearing concepts, integration into a mega-Watt scale oil-free rotor system and demonstrating reliable operation is needed.

The turbomachine concept in Figure 2c also poses unique challenges with thermal system design. With the high fluid density of sCO_2 and the high rotor speeds, windage-generation from bearings, on rotor surfaces, and cavities becomes a major risk.

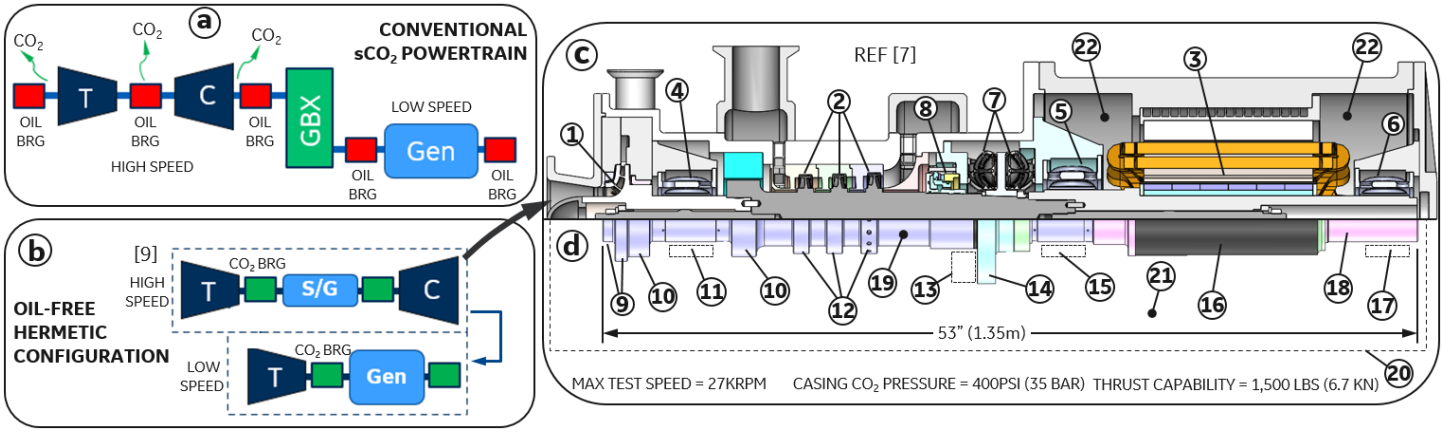

Fig 2. Oil-free drivetrain and test rig rotor concepts: (a) conventional sCO_2 power train, (b) dual-spool oil-free hermetic power system [9], (c) conceptual design of high-speed gas generator for a sCO_2 WHR unit [7], (d) simplified test rotor for reducing technology risks. (1) 3.87MW centrifugal compressor, (2) 4.83MW 3-stage turbine, (3) 1MW starter-generator, (4) compressor -end radial bearing, (5) mid-span bearing, (6) generator-end bearing, (7) thrust bearings, (8) film-riding seal, (9) rotor-steps simulating the centrifugal impeller inertia, (10) balance piston, (11) compressor bearing location, (12) rotor-steps simulating turbine, (13) thrust bearing location, (15) midspan radial bearing location, (16) 1MW starter-generator, (17) generator-end radial bearing location, (18) permanent magnet electric machine shaft, (19) turbo-compressor shaft, (20) hermetic CO_2 pressure boundary, (21) 400psi CO_2 environment, (22) electric machine cavity

Bearing windage, especially for the thrust bearing, generates heat and can create high temperatures leading to thermal distortions that are detrimental to the lubricating gas film. Windage heat generation in the magnetic rotor gap (of the starter-generator) and the cavity temperatures, where the end windings reside, are other locations that need to be addressed. Therefore, in efforts to minimize heat generation and temperatures, the concept in Figure 2c uses a film riding seal to isolate the electric machine cavity and most of the bearing system into a dedicated lower pressure CO_2 control volume. The leakage from the high-pressure turbine exhaust cavity to the lower pressure electric machine cavity occurring past the seal will be driven by a separate leakage re-compressor. This approach was also used by Conboy et al. [16] where they used a scavenging booster pump to evacuate the rotor cavity and drop cavity pressure to 300 psi (2.06 MPa) [17] in efforts to prevent high friction losses. Foil bearing temperatures were reported to reach 315-550C [17]. More recently a 2018 paper by Miller et al. [23] presents rotating testing on a 1.5 MW permanent magnet motor-generator rotor system. The work looks at a sCO_2 turbomachine concept, where the electric machine is operating in a lower pressure CO_2 environment, like Conboy et al. [16]. Testing was conducted at 0.7 MPa and a max speed of 25krpm, while supporting the rotor systems using oil-lubricated ball bearings. The authors used a semi-sealed alternator cavity and a pressure control system to maintain the 101-psi (0.7 MPa) operating condition.

The high-speed turbine-compressor with a starter-generator [7] shown in Figure 2c has four technical risks that need to be mitigated with full-scale experimental demonstration. These risks include (a) thrust bearing load capacity, (b) dynamic load capability of radial gas bearings, (c) high-speed rotordynamics of an oil-free rotor system, and (d) thermal management of the bearings and electric machine immersed in a high-pressure CO_2 environment. The main goal of this work was to present an equivalent test rig rotor system engineered to reduce these critical risks associated with a sCO_2 hermetic oil-free power drivetrain. Since compressor and turbine sCO_2 technologies have been developed in past work [10-12], the test rig looks to use a simplified rotor design (Figure 2d) without a compressor stage or turbine section to address the remaining risks with the concept. The test rig will use novel additively manufactured externally pressurized

gas bearings while having the capability to apply thrust, assess rotordynamics, and benchmark thermal models. The remainder of this report is arranged as follows: Section 2 describes the test rig design process and cross-section. Sections 3 and 4 describe the electric machine design and the permanent magnet rotor assembly respectively. The rotor-bearing system design and rotordynamics are discussed in Section 5 and 6 respectively, with the conclusions presented in Section 7.

2. TEST RIG DESIGN PROCESS AND CROSS-SECTION

The design considerations and conceptual design process for the turbomachine layout in Figure 2c is described in the reference paper [7]. Since the test rig discussed in this report simulates the turbomachine layout of Figure 2c, the test vehicle design process closely mirrors the design process in Ertas et al. [7]. Specifically, the design effort in reference [7] set requirements for general rotor geometry, electric machine specifications, operating speed, bearing loads, and ambient operating pressure. The test rig design described in this report uses these requirements as boundary conditions for the different design elements and is shown in Figure 3. The test rig design task consisted of four main areas of focus including component design, rotordynamics, thermal system analysis, and centerline drivetrain layout. To achieve an optimal design, an iterative approach was required between the shared boundary conditions amongst different design elements. In this report only the mechanical and electrical design details will be presented. A second reference paper [24] focuses on the thermal system design of the test rig and the CO_2 flow loop.

A couple of relevant references are by Miller et al. [23], previously discussed, and Wilkes et al. [25]. The work in reference [25] looked to evaluate a gas foil thrust bearing up to 120krpm in a 69-bar high-pressure nitrogen environment using a 22kW powered test rig. They used a simple test rotor directly coupled to a turbocharger for driving the system and a pressurized gas chamber for creating axial thrust up to 300lbs. The test rig was quite capable, being able to apply varying thrust, assess thrust bearing load capacity, and calculate power loss. The current test rig looks to leverage concepts from both Miller et al. [23] and Wilkes et al. [25], while adding the capability of evaluating radial bearing damping through rotordynamic unbalance testing.

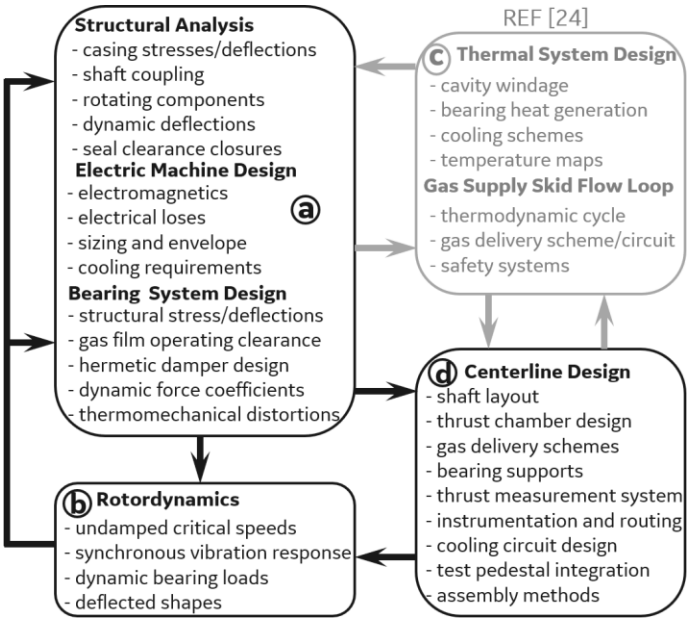

Fig 3. Test rig design process: (a) component design, (b) drivetrain rotordynamics, (c) thermal system design [24], (d) centerline design

The general test rig side view is shown in Figure 4 and the cross section of the test rig is presented in Figure 5. The test rig platform uses two upright pedestals that are bolted to a t-slot test table. The pedestals are used to support and position the casing assembly, which is comprised of the turbo-compressor casing and the motor-generator casing. The test rig utilizes a hermetically constructed casing and CO_2 flow loop, leading to a leak-proof closed cycle system. Access hatches are designed into the casing for access to instrumentation, to support assembly steps, and to allow access to rotor balance planes.

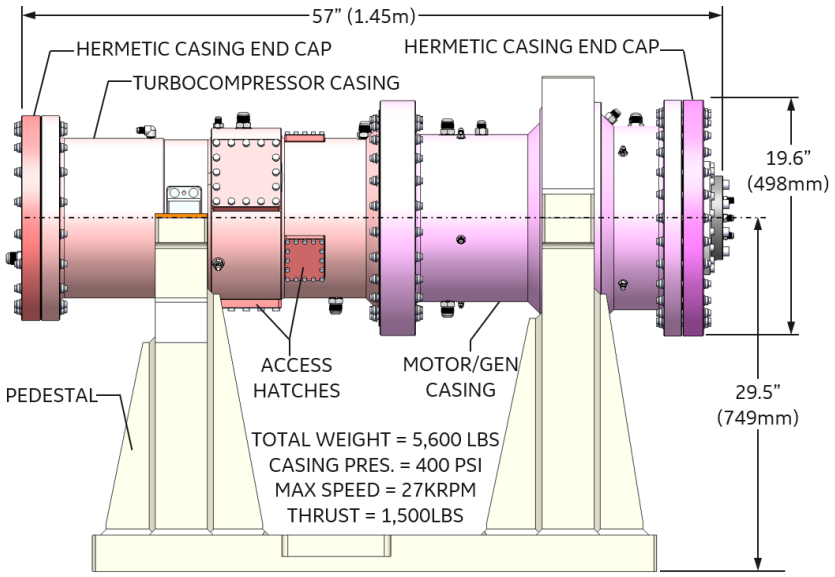

Fig 4. Test rig side view and general dimensions

One of the unique aspects of the test rig architecture was the implementation of a 3 bearing rotor system to increase power density and minimize parasitic friction losses. The rotor is constructed using the turbo-compressor shaft and the generator shaft, which are coupled through a relatively stiff mechanical joint. Since this test rig is not evaluating the turbomachine aero stages, the compressor section and turbine section are designed to have equivalent geometry emulating the centrifugal compressor and 3-stage axial turbine from reference [7]. A decision was made to remove the compressor tie rod from the original concept and use an integral shaft element. This change simplified rotor design but necessitated that the compressor-end radial bearing be horizontally split. The midspan bearing and generator end bearing however, are 360-degree components. The thrust bearing is shown in the center of the rotor assembly reacting thrust from the rotating thrust runner. All bearings and bearing supports were fabricated using direct metal laser melting (DMLM). The motor-generator rotor uses permanent magnets that are secured in place during operation using an interference fit carbon fiber retaining sleeve. There are several CO_2 inlets and outlets to the casing. First, there are 4 external inlets to pressurize the gas bearings. Second, there are cooling inlets that deliver cooling flow to critical locations such as bearing cavities, electric machine cavity, and the magnetic gap in the electric machine. Water cooling is also used in this test rig concept through a cooling jacket on the outer diameter of the electric machine armature. Lastly, there are exit ports in three locations that extract hot CO_2 from the hermetic casing. More information on the secondary flow circuit can be found in reference [24].

The instrumentation for the test rig was chosen to assess and retire risks and was also used for health monitoring. Rotor speed will be monitored using a non-contact proximity probe as a key phasor and rotordynamic vibration orbits will be measured using X and Y proximity probes located at 4 different measurement planes.

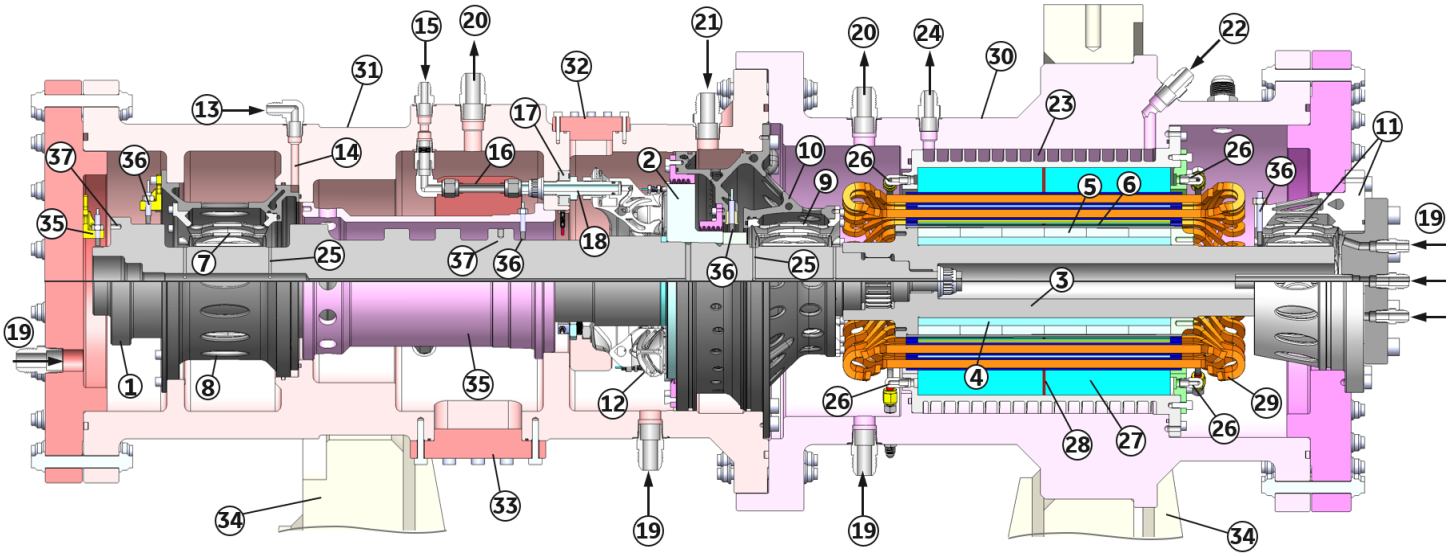

Fig 5. Test rig cross-section: (1) simulated turbo-compressor rotor, (2) thrust runner, (3) motor-generator shaft, (4) laminations, (5) rotor magnets, (6) carbon-fiber retainment sleeve, (7) compressor-end radial bearing, (8) compressor-end bearing housing. (9) midspan radial bearing, (10) mid-frame housing. (11) generator-end bearing with integral housing, (12) thrust bearing, (13) hydrostatic pressurization inlet for compressor-end bearing, (14) radial inlet hole to housing, (15) hydrostatic pressurization inlet for thrust bearing, (16) gas delivery circuit to thrust bearing, (17) axial force load cell, (18) gas delivery thrust shank, (19) cooling CO_2 flow inlets, (20) hot CO_2 flow exit, (21) thrust chamber pressurization inlet, (22) H_2O inlet, (23) H_2O cooling jacket, (24) H_2O exit, (25) radial cooling holes, (26) CO_2 inlets for magnetic gap cooling, (27) stator armature, (28) midspan lamination stack cool gas delivery to magnetic gap, (29) electric machine end windings, (30) electric machine casing, (31) turbo-compressor rotor casing, (32) small access hatches, (33) large access hatches, (34) pedestal supports, (35) key-phasor, (36) rotor vibration probes, (37) unbalance-weight plane

Proximity probes are also used on the thrust bearing to monitor vibrations and operating gas film thickness values. Load cells are implemented at the thrust bearing housing mounts for measuring axial thrust loads. Pressure transducers and thermocouples will be used for monitoring CO_2 conditions in machine cavities and gas bearing inlets. The CO_2 flow through the test rig and bearings is powered by a gas supply system (GSS). The GSS is a closed CO_2 flow loop that will maintain the test casing internal pressure at 400 psia (27.6 Bar), while supplying high pressure CO_2 to the test casing components including the bearings, the rotor thrust system, and the cooling flow circuit. The GSS is a separate stand-alone skid controlled by an in-house designed control system but with on-board control capability to shut down the test system safely when necessary. The GSS consists of high-pressure CO_2 tanks that are used to charge the system and are responsible for maintaining adequate CO_2 mass-flow through the closed flow-loop during the test. The GSS uses one high-pressure gas booster and seven low pressure gas boosters that are used to raise the pressure of the CO_2 in the supply tank to levels sufficient to drive the necessary mass flows. These pneumatically driven gas boosters are activated by 144-psia (9.9 Bar) compressed air and operate at 50 cycles per minute. The HP manifold supplies pressurized CO_2 gas to the thrust bearing

feed line while the LP manifold distributes pressurized gas to the radial bearings, the thrust chamber, the EM magnetic gap cooling, and cavity cooling lines. More details of the GSS can be found in reference [24].

3. ELECTRIC MACHINE DESIGN

This section outlines the electric machine design and how it was modified from the previous study [7] to meet test rig requirements. As discussed previously, the test rig rotor system excludes the compressor and turbine aero stages and thus lacks the ability to drive the rig through turbine power. Therefore, the electric machine in the test rig was designed to operate as a motor to drive the system to maximum speed of 27krpm. Hence, the following analysis looks to modify the test rig electric machine to match critical parameters to reduce risk for the full scale 1 MW machine. The power rating for the prototype electric machine was calculated based on the system windage loss, and the acceleration requirement, as below:

Machine power rating = (System windage loss + acceleration power)*FOS,

where FOS is the factor of safety. In early stages of system design, the system windage loss was calculated as 77kW and the acceleration power requirement was calculated based on the following:

- Acceleration from 0 – 27,000 rpm in 2 minutes
- System polar moment of inertia = 2 kg-m2
- Constant torque during startup

This results in a start-up torque of 47Nm and gives a total power rating 210 kW. Considering a FOS of approximately 1.4, the power rating for the prototype is fixed at 300kW, at a speed of 27krpm. The 1MW electric machine armature design from the earlier design effort [7] was modified to provide 300kW. To simulate representative rotordynamics behavior for the 1MW design, the machine stack configuration and rotor diameter were left unchanged. The reduction in power rating from 1MW to 300kW was accomplished through a change in the stator outer diameter. The modified stator was analyzed using a two-dimensional finite element analysis (electromagnetic simulation) to verify the performance of the machine (Figure 6). The loss distribution shows that the windage loss far exceeds the copper and core loss (Figure 7). A separate script considering the properties of pressurized CO_2 (400 psi) was used for the calculation of windage loss. The machine is indirectly cooled through a jacket on the stator outer diameter. A preliminary thermal analysis showed that considerable winding heating was caused due to the high windage loss (Fig. 3). To mitigate this, cooling flow was introduced in the magnetic gap. More information on the thermal performance and role of magnetic gap cooling are discussed in the reference paper [24] The ongoing work includes preparation of a specification for VFD manufacturers (Table 1) and implementing novel cooling solutions for the machine [24].

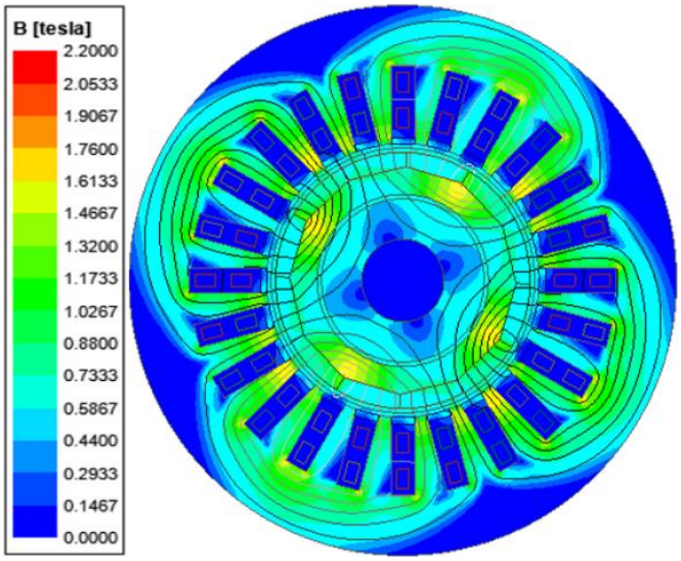

Fig 6. Electromagnetic flux paths from 2D FEA

Table 1. Electric machine parameters for VFD

Number of poles	Current [A]	Voltage [V]	Magnet flux [Wb]	Phase resistance [mohm]	Ld [micro-H]	Lq [micro H]	Rated speed [rpm]	Rated frequency [Hz]	Machine rating [kW]
4	412	480	0.0631	4	36.5	36.2	27000	900	300

Other changes made include (Fig. 7):

- Rectangular stator slots for ease of winding
- Increase the number of stator slots from 12 to 24

To improves thermal performance and reduces harmonic content in the air gap field for lower rotor and magnet loss.

MACHINE CONFIG	REF [7]	CURRENT
Max operating speed [KRPM]	27	27
Torque [Nm]	369	110
Power [MW]	1.0	0.31
Number of coils	6	24
Copper loss [W]	2532	2257
Stator core loss [W]	5000	3900
Rotor core loss [W]	100	0.59
Friction and windage loss [W]	7690	7750
Axial stack length [mm]	268	274
Magnet stack outer diameter [mm]	114	114
Line current [A]	N/A	412
3-Phase voltage [V]	N/A	457

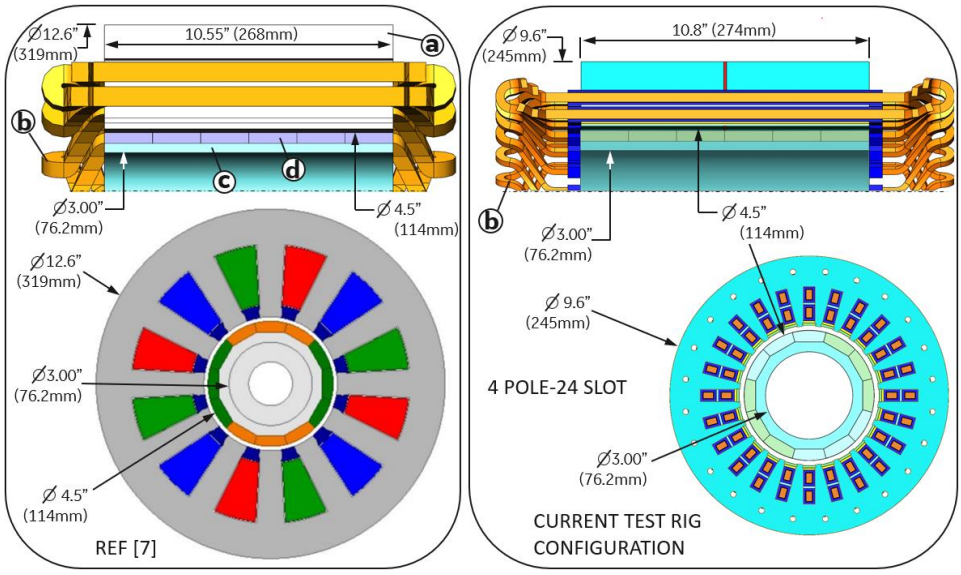

Fig 7. Electric machine design: Design from [7] versus current machine design

The stator winding is designed for a 3-phase voltage of 480V rms. The winding insulation system corresponds to a higher voltage level of 4160V, to ensure that the 300kW prototype more correctly represents the thermal resistance of the full-scale 1MW generator (Table 2). The winding has 4-poles, and 4 parallel paths. Each coil has 3-turns, made of rectangular compacted Litz wire to minimize the supplementary ac loss. The windings are distributed and have 2 slots per pole per phase (Fig. 7). The stator is made from Vacodur-49 laminations (from Vacuumschmelze), while HF10 from AK Steel is used for the rotor material. The shaft is made from high strength magnetic steel. The rotor has 4-poles, and has a surface mounted permanent magnet construction. Carbon fiber is used for the retaining sleeve.

Table 2. Winding insulation build used in the 300kW, 480V prototype

Generator voltage [V]	4160
Strand insulation (polyimide enamel) [mil]	2
Turn insulation (mica tape) [mil]	15
Groundwall (mica tape) [mil]	85
Conducting armor tape (carbon filled FG) [mil]	10
Phase separator [mil]	80
Wedge and top filler [mil]	150

4. PERMANENT MAGNET ROTOR ASSEMBLY

The rotor assembly, shown in Figure 8, consists of four concentric 'rings' which are almost always assembled sequentially from the innermost to the outermost component, each having directionally oriented mechanical properties. In this design, the innermost component is a solid shaft (with isotropic properties), which serves as the foundation of the rotor assembly and provides most of the lateral bending stiffness in the rotor assembly. The second ring is a steel, axially laminated rotor core that enhances the field in the magnetic circuit but has anisotropic mechanical properties with very little structural contribution in the axial direction. The third ring is comprised of discrete permanent magnets, which are segmented in the circumferential (hoop) direction and the axial direction and treated as an unsupported mass in the rotor assembly. The fourth ring is a carbon fiber retaining ring with high stiffness and strength in the circumferential direction, but moderate stiffness and strength in radial and axial directions. This unique series of stacked-up elements with anisotropic mechanical properties provides interesting opportunities and challenges to the design engineer.

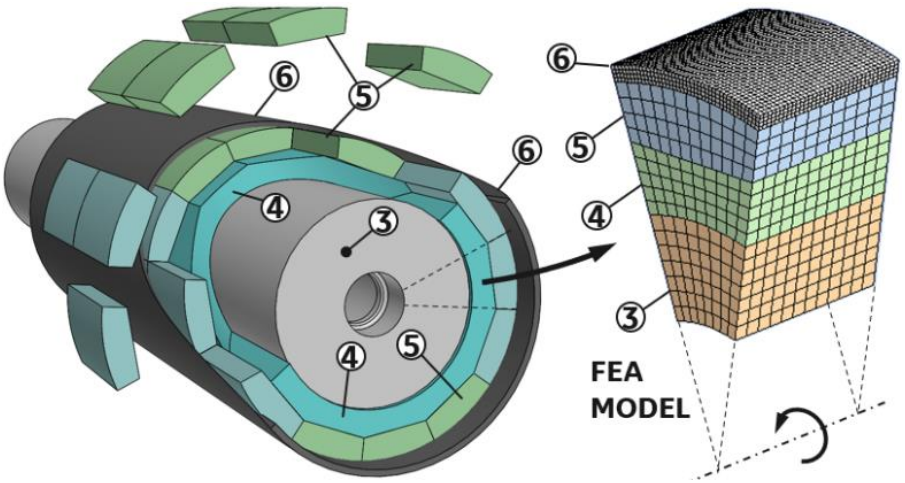

Fig 8. Permanent magnet rotor construction and FEA: (3) rotor shaft, (4) laminated rotor core, (5) magnets, (6) carbon fiber retaining ring

There are several key design criteria that must be achieved in the rotor assembly. The first is to maintain sufficient interface pressure between adjacent components, also known as radial preload or radial stress. Radial pressure is achieved by assembling adjacent components with diametral interference, usually through the application of shrink fits by heating the outer part and chilling the inner part. Sometimes press-fits are used, but less frequently than shrink fits. The radial interface pressure is evaluated under all possible conditions, considering component temperature, manufacturing tolerances, and rotational speed. An example of combining mechanical and thermal loads and the resulting radial stress is shown in Figure 9.

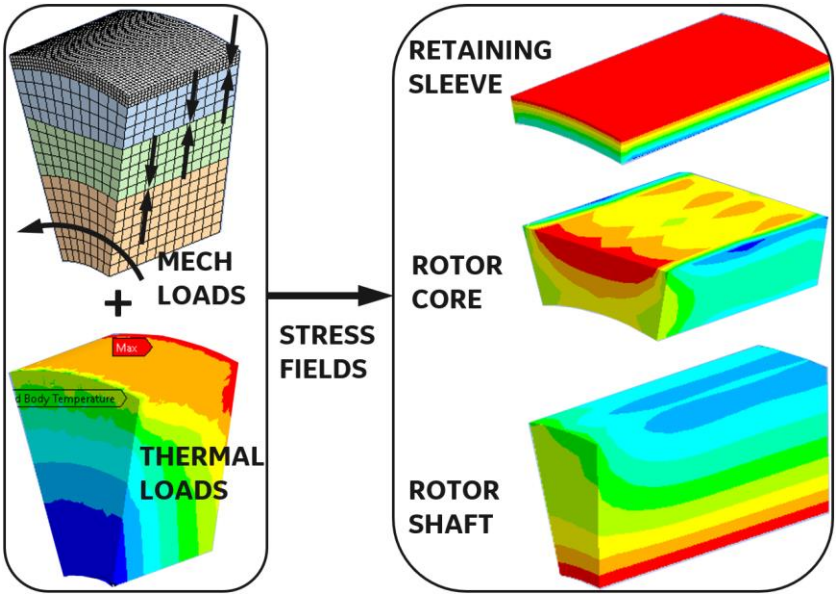

Fig 9. Magnet stack thermomechanical stress fields

The minimum allowable interface pressure is determined by the amount of torque that needs to be transferred through the interface, but often falls in the range of 500-1000 psi. If interface pressure is insufficient, the rotor components may slip relative to one another or result in an unexpected increase in unbalance, both of which are undesirable.

Component stress is the second design criterion that is considered. The rotor components are stressed while at room temperature and stationary, due to the assembly approach described earlier. Frequently, the stress in most components increases with speed and temperature, forcing the design engineer to find the balance between assembly stresses and operating stresses without exceeding the allowable stress for each of the rotor materials. For a rotor assembly with a long service life requirement, the material fatigue strength can dictate the allowable stress.

The third key design criterion are the rotordynamics of the rotor assembly. The anisotropic material properties of the rotor assembly means that the rotor shaft often provides most of the lateral stiffness. Additionally, the discrete magnets mostly contribute mass to the rotor system and play an important role in the critical speed calculation. The rotor assembly used in the electric machine is included in the system level rotordynamics model as shown in Section 6 of this report.

5. ROTOR-BEARING SYSTEM DESIGN

The design for the rotor, bearings, and supports involved a holistic analysis approach, which included mechanical, thermal, and dynamic effects in the test rig system. Figure 10 shows the thermomechanical finite element (FE) model for the rotor and the stationary components with loading conditions such as fluid pressures, centrifugal loads, interference fits, bolt

preloads, rotordynamic shaft deflected shapes, and the temperature map from Bidkar et al. [24]. In addition to the FE model, the design required the use of specialized component analysis design tools for bearings, dampers, and rotordynamics. This section aims to accomplish several goals. First, the rotor-bearing system design is reviewed in detail. Second, additive manufacturing feasibility is assessed through prototype build trials and section cut ups. Lastly, design loops are highlighted and discussed for the bearing-rotor systems.

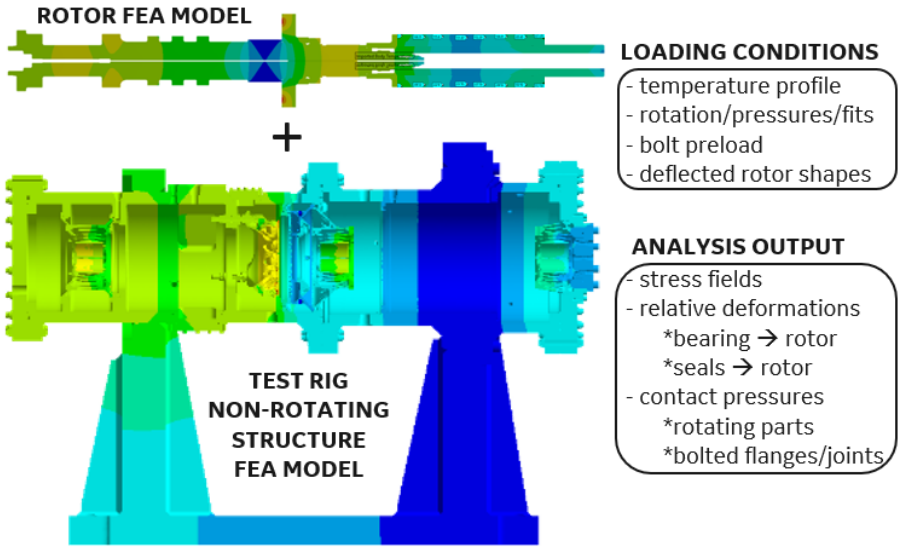

Fig 10. Thermomechanical system analysis

The rotor-bearing system design requirements included ability to apply thrust, measure thrust, deliver pressurized gas to bearings, and have necessary instrumentation to assess the key risks in a 400-psi (27.6-Bar) CO_2 environment. The design also looked to implement additive manufacturing beyond bearing systems and therefore all bearing supports were designed for DMLM. The rotor-bearing system, isolated from the test rig, is shown in Figure 11 and is comprised of 2-shaft rotor assembly supported by radial gas bearings and a thrust bearing. The two shafts are mechanically coupled together using interference lands for establishing concentricity and moment stiffness, a spline connection for transmitting torque, and a preloaded central integral bolt to clamp the joint.

The key enabling technology for the proposed oil-free hermetic turbomachine concept is the bearing system. The main consideration when conceiving the bearing design was the ability to scale to large power machines. Hence the bearing system uses externally pressurized CO_2 to provide high load capacity, engineers a compliant pad support for sustaining misalignment, and implements a novel hermetically sealed squeeze film fluid damper in the bearing. The bearing design concept can be categorized as a "soft-mounted" bearing system. Soft-mounted rotor-bearing systems are common in aircraft gas turbine engines [26], centrifugal gas compressors [27-28], and ground-based power turbine applications [29-33]. More recently, Moore et al. [10] successfully tested a soft-mounted 10MWe sCO_2 turbine rotor system on integral squeeze film dampers to 27krpm. In all these systems, a rolling element bearing, or oil-lubricated fluid-film bearing is "soft-mounted" in series with a stationary flexible bearing support, which also possesses a squeeze film fluid damper [34]. This bearing support design philosophy in principle is applied to the current gas bearing concept and is shown in Figure 11. The effectiveness of the concept relies on a carefully engineered stiffness ratio between the bearing gas film and the flexible bearing support (Figure 12). As shown in Figure 12 the bearing can be conceptualized as a fluid-film in series with a stiffness and damping element that represents the pad support. The stiffness ratio between the two bearing elements not only

influences location of natural frequencies, but also controls the equivalent “damping-to-stiffness” ratio of the overall bearing-support system. Due to the high number of functional requirements for the radial bearing, additive manufacturing was chosen for the design and manufacturing approach. Additive manufacturing has been implemented to gas bearings in previous work by Ertas [35], where experimental rotating tests on a 6.8 in. (173 mm) diameter externally pressurized thrust bearing fabricated using DMLM were performed. The thrust bearing concept was designed using individual bearing pad modules with independent compliant degrees of freedom for sustaining misalignment. The current radial bearing design leverages the individualized pad module concept, however, it incorporates a new HSFD [36, 37] design and a different module connection approach appropriate for lateral rotor support. The radial bearing configuration in Figure 11 contains four pad modules that are rigidly connected through inter-pad webs. These interface webs provide hoop stiffness to the assembly, while the 360° mounting flanges react bearing loads to the machine casing.

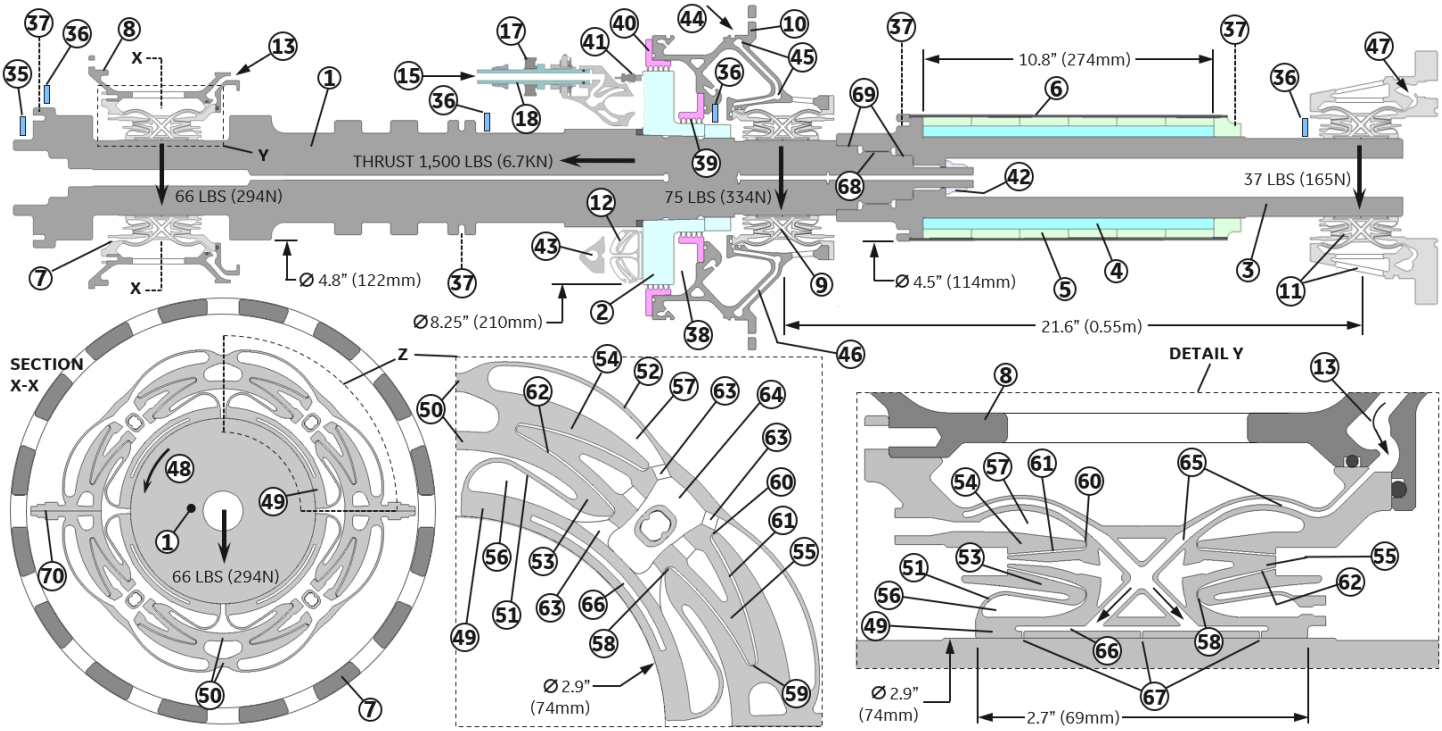

Fig 11. Rotor-bearing-support system and radial bearing design concept: (38) thrust chamber, (39) small laby seal, (40) large laby seal, (41) film probe, (42) central shaft tie nut, (43) thrust bearing housing inlet gas plenum, (44) hydrostatic pressurization inlet flow into midspan bearing (inlet not shown), (45) annular distribution plenums, (46) fluid transfer channel between annular distribution plenums, (47) hydrostatic pressurization inlet flow into generator bearing, (48) shaft rotation, (49) radial bearing pad, (50) inter-module web, (51) lower diaphragm, (52) upper diaphragm, (53) lower support jaw, (54) upper support jaw, (55) damper plunger, (56) lower accumulator cavity, (57) upper accumulator cavity, (58) lower accumulator flow restriction, (59) damper plunger flow restriction, (60) lower accumulator flow restriction, (61) upper damper cavity, (62) lower damper cavity, (63) pass-through channel flow-port, (64) pass-through channel, (65) hydrostatic flow delivery jacket, (66) pad labyrinth, (67) hydrostatic orifice holes, (68) shaft interface lands, (69) shaft spline connection, (70) compressor-end bearing horizontal split-line

The pad module design cross-section is shown in Figure 11 and is comprised of either compliant members or structural components that were designed with high-stiffness intent. The moving pad body is constructed by integrally combining the bearing pad, pad central post, and plunger design elements. This "rigid" body interfaces with the stationary outer bearing shell through two flexible diaphragms. One diaphragm is designed from the outer bearing pad perimeter to the lower support jaw. The other compliant spring connects from the central pad post and merges with the bearing shell near the inter-pad web connections. To generate high levels of load carrying capability, the design in Figure 11 uses CO_2 at 540-psi (37-Bar) for external pad pressurization to create a hydrostatic operating film. Hydrostatic pressure is introduced at the pressurized gas inlet where the flow traverses through an axially oriented gas delivery jacket contoured to the inside surface of the outer compliant diaphragm spring. This high-pressure gas is then transferred to the pad labyrinth where it is finally delivered to the operating bearing film gap through an orifice hole on the face of the pad. The HSFD in this design possesses 4 distinct fluid volumes that include 2 damper cavities and 2 accumulator cavities. The two other accumulator cavities are connected by a non-restrictive pass-through channel, whereas the damper cavities have fluid communication through the plunger tip restriction gap. A companion reference [36] discusses the new HSFD design in detail and presents dynamic testing results. For the current test rig, rotor vibration probes (shown in in Figures 5 and 11) in combination with radial bearing pad thermocouple (TC) measurements will be used to assess the performance of the bearing system.

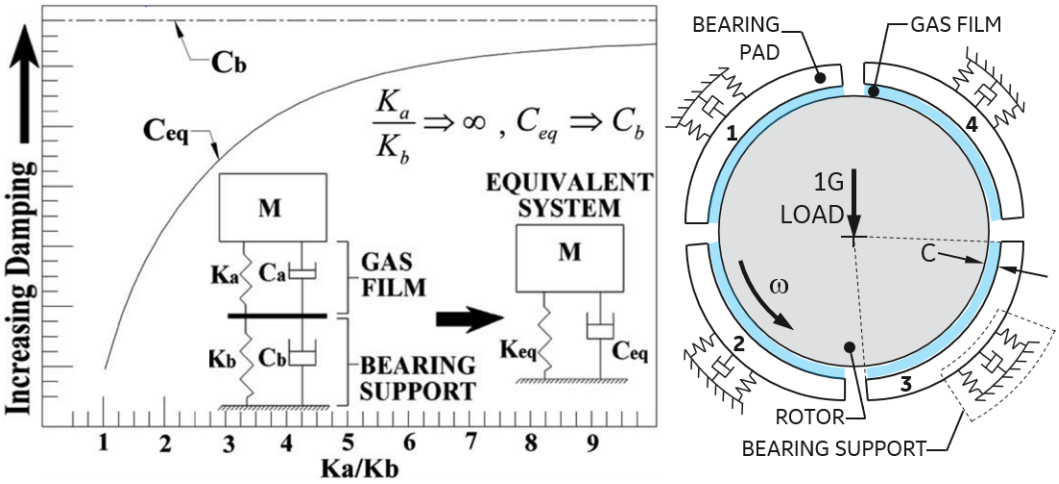

Fig 12. Flexibly damped gas bearing system: Effect of soft-mounting and stiffness ratio on equivalent bearing system damping

To further improve reliability and reduce cost all bearing supports in the design are envisioned to be additively manufactured using DMLM. The support housings are responsible for positioning the bearings and reacting loads to the casing. They also serve the function of delivering high pressure CO_2 to the bearings and are used to create a thrust chamber for generating rotor thrust. All bearing supports utilize an integrally designed internal gas delivery channel that routes high pressure CO_2 from the outer casing to the bearing using a minimum number of parts. Having the ability to additively manufacture a design is no doubt a major enabler for innovative solutions that would otherwise not be feasible

with conventional manufacturing methods. However, realizing highly complex geometries is not a trivial task. Therefore, a major risk with the proposed design was the ability to produce high-quality additively built components. Figure 13 shows additive build trials for the radial bearing and the compressor end housing. Several iterations of additive builds were performed followed by cut-up analysis of the components. For the bearing system, verifying precise control of internal clearances without unintended fusing was a major area of focus. Critical clearances include the plunger tip clearance and accumulator clearances, as shown in Figure 13. The compressor-end bearing housing in Figure 13d also reveals internal build quality for the internal ports and annulus.

The thrust application and measurement system are other critical elements to the test rig objectives and are shown in Figures 14 and 15. The thrust chamber was designed using two labyrinth seals and a pressurized cavity that reacts a pressure load on the rotating system. The two seals are installed on the outer-diameter and inner diameter of the rotating thrust runner, which creates an axial pressure area for the thrust load. High-pressure CO_2 at 430-psi (29.6-Bar) is introduced into the chamber generating an axial thrust of 1,500-lbs (6.7 kN) on the thrust runner. The thrust load is then reacted by a 9-pad externally pressurized gas thrust bearing manufactured using DMLM. The thrust bearing design is copied from reference [35], however incorporates 9 pad modules instead of 8 and has a customized integral housing design for interfacing with the thrust measurement system.

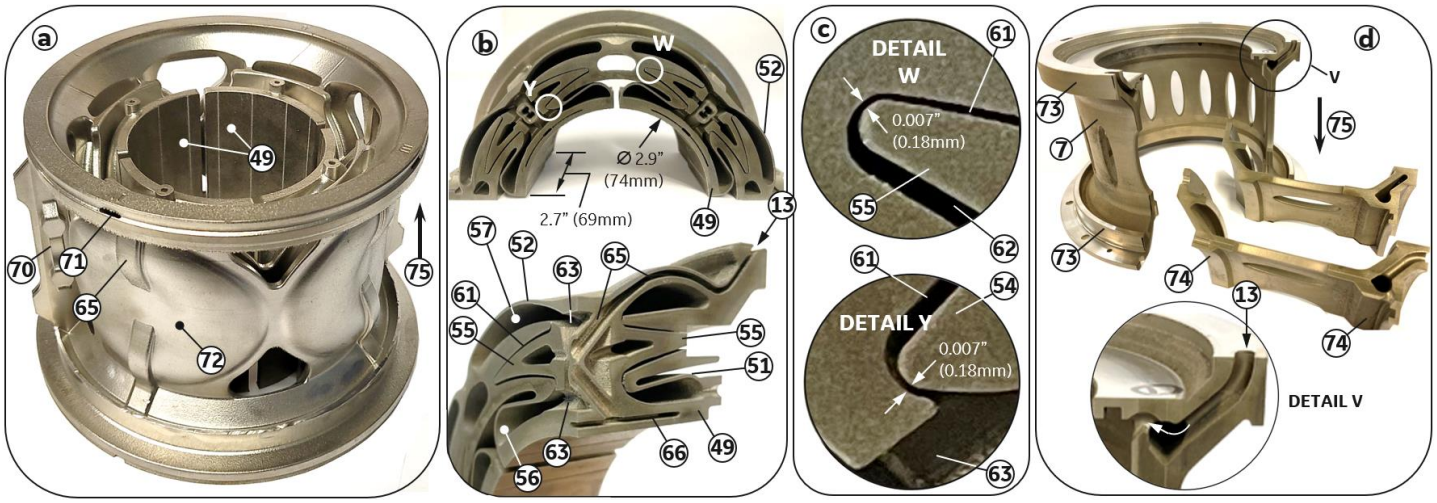

Fig 13. Inconel 718 compressor end radial bearing and support DMLM build trials: (a) additively built compressor end radial bearing (b) additive build cut ups, (c) damper clearance close-ups, (d) compressor bearing housing build and cut-ups, (71) hydrostatic gas delivery slot, (72) pad module, (73) housing to casing assembly lands, (74) bearing to housing assembly lands, (75) additive build direction

The thrust load from the bearing face is reacted through three mount points on the thrust bearing backing flange and interfaces with the gas delivery thrust shank. Each of the three thrust shanks transfer load from the thrust bearing to three load cells installed in internal flange pockets inside the turbo-compressor casing. Furthermore, the shank is used to deliver

820-psi (56.5-Bar) CO_2 to the thrust bearing. By combining these two functions in the gas delivery thrust shank the design eliminates potential parallel load paths and maximizes the thrust load measurement accuracy.

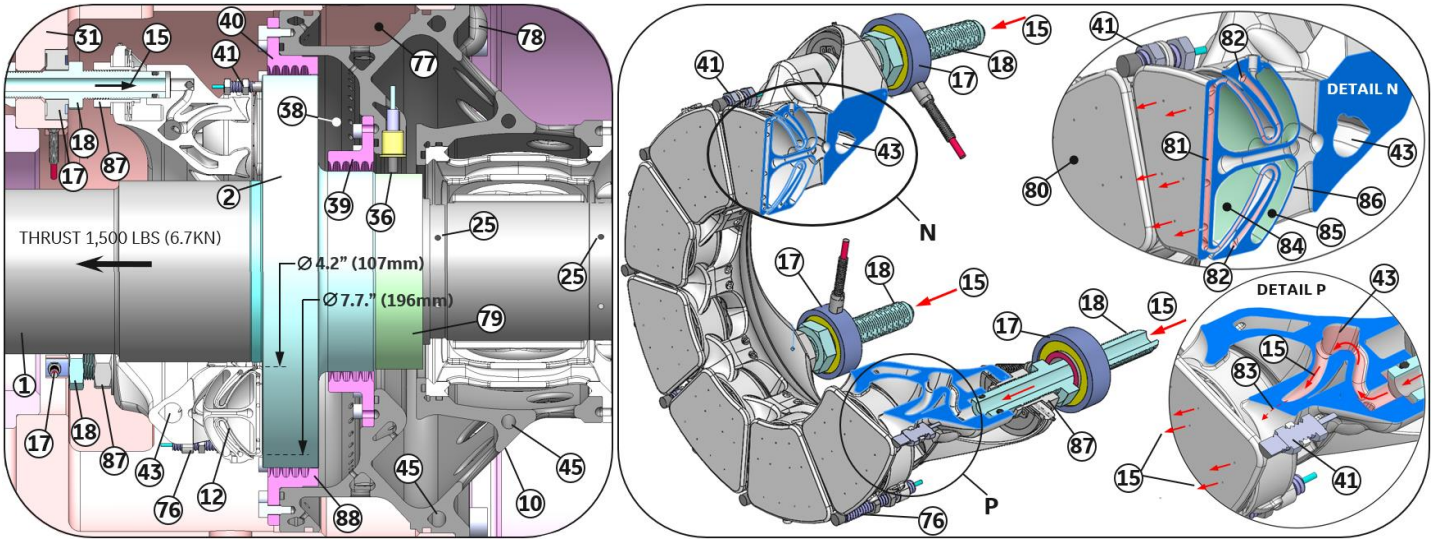

Fig 14. Thrust application system and thrust bearing detail: (76) housing probe, (77) high pressure inlet plenum, (78) hydrostatic inlet port on midspan housing, (79) thrust runner spanner nut, (80) bearing pad thrust face, (81) pad labyrinth, (82) bearing shell annular distribution plenum, (83) inlet flow penetration to bearing shell annular distribution plenum No. 82, (84) forward side damper fluid cavity, (85) aft side fluid cavity, (86) aft side diaphragm, (87) thrust bearing housing lock-nut, (88) swirl brake

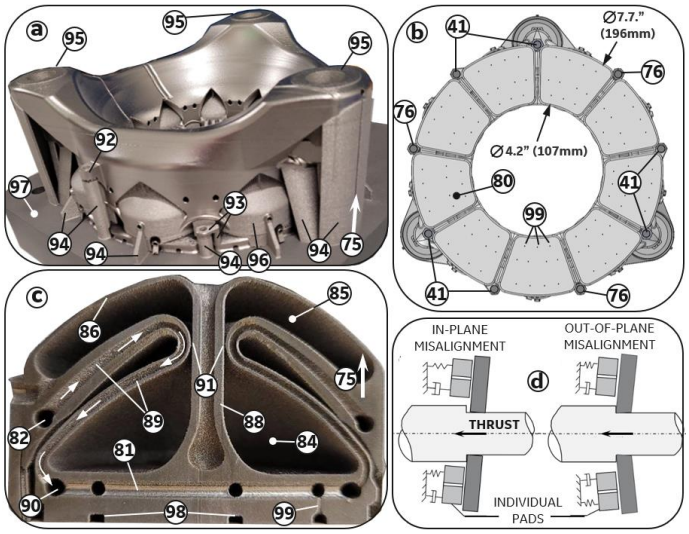

Fig 15. Inconel 718 thrust bearing build and concept: (a) full 360° thrust bearing build, (b) front view of 9-pad thrust bearing, (c) thrust pad module cut in half. (d) thrust bearing misalignment capability (88) pad post, (89) gas delivery passage, (90) thrust pad annular distribution plenum, (91) damper clearance, (92) housing probe mount, (93) pad film

probe mount, (94) build supports, (95) thrust housing mounting land, (96) thrust pad module, (97) additive build plate, (98) power removal grooves, (99) high-pressure gas delivery orifice on thrust face

The thrust face is segmented into different pad surfaces and individual pad modules so that static misalignments and out-of-plane misalignments can be absorbed by the bearing system. Each pad module is designed with a high axial stiffness but possesses flexibility in the rotational degrees of freedom of the pad. This is different from the radial bearing approach were the translational degree of freedom to the pad (radial direction) is designed to be flexible due to rotordynamics. Gas is delivered into the housing and utilizes an annular inlet plenum to distribute gas to individual pad modules. Pressurized CO_2 then penetrates the pad module through an array of integral delivery passages that contour the flexible diaphragm springs, transferring pressurized gas from a stationary reference frame to a complaint moving pad. The thrust bearing pad module also incorporates an older version of HSFD just to ensure a positive stability margin in the axial direction. The combination of compliance in a circumferentially segmented thrust face, external pressurization, and the use of additive manufacturing enables scalability of the thrust bearing concept to high-powered turbomachinery. To assess the performance of the thrust bearing during testing three displacement probes are installed on the thrust bearing housing, 3 pads are instrumented with corner point displacement probes, and TCs are applied to the pad corners. The housing probes give an indication of thrust runner motion and position with respect to the housing whereas the pad probes are used to assess gas film operating clearance (gap). Using these motion probes in combination with the thrust measurements, gas film properties like stiffness and minimum operating gaps can be benchmarked with design tools [38].

The engineering analysis that drove the radial and thrust bearing designs required an integrated design loop amongst several design tools and disciplines. To address the risks, design loops for the radial bearings were performed as shown in Figure 16. There were three main areas of focus. First, an in-house bearing design tool was used to act as the interface between rotor and stator structural FEA models (as shown in Figure 10). The bearing design tool, developed by Delgado [39], is a Reynolds based analysis tool that outputs steady state operating conditions for the gas film and calculates equivalent speed and frequency dependent bearing force coefficients for rotordynamic analysis. The tool is based on an iso-thermal compressible laminar flow model suited for an ideal gas and can impose angular misalignments between rotor and bearing surfaces. The second element focuses on the HSFD analysis and involves creating a fluid-structure-interaction (FSI) model of the bearing support, as described in [36].

This model is comprised of a computational fluid dynamics analysis (CFD) of the damper fluid using a 2-way coupling with a transient structural FEA model of the structure. Damping is assessed for multiple frequencies and clearances conditions to target the damping requirement. The final element in the radial bearing design is the assessment of the bearing structure. The loading conditions imposed on the pad and structure are either static loads or alternating loads. Effects such as misalignment, rotor weight, relative deflections of the rotor versus stator are ultimately applied to the bearing pad through a pressure profile from the Reynolds bearing tool. This static stress condition is then complemented with dynamic loads coming from rotordynamics to assess high cycle fatigue and ensure reliable life of the component.

The thrust bearing design process (Figure 17) incorporates similar elements as the radial bearing with less emphasis on dynamics and more emphasis on relative bearing to thrust runner distortions. The thrust gas bearing design tool [38] is an extension of the radial gas bearing tool and possesses all the same modeling assumptions and capabilities. In the design process for the thrust bearing careful consideration is given to the relative distortion between the thrust runner and the bearing thrust face.

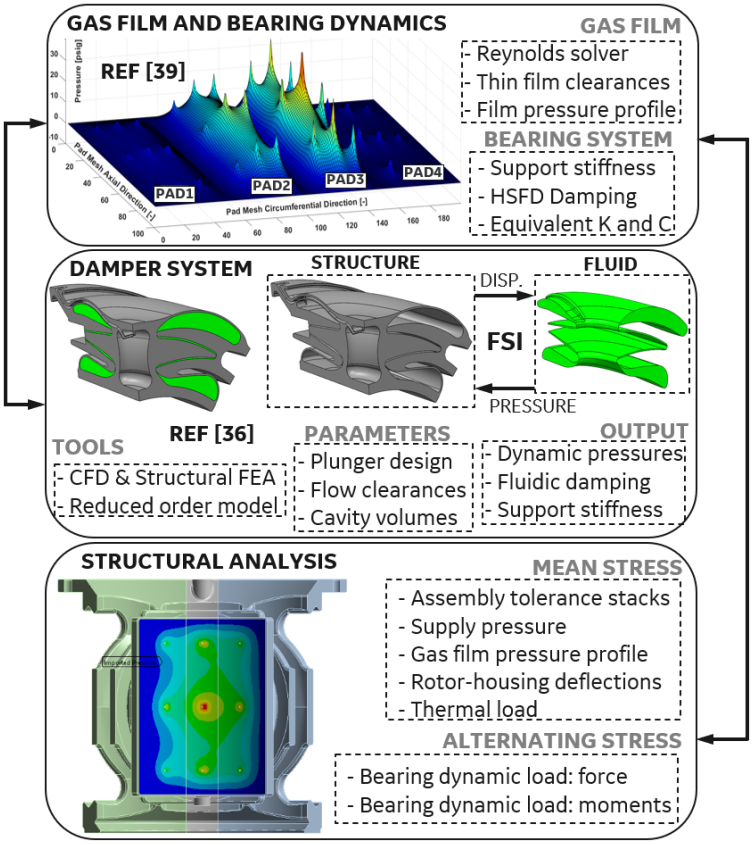

Fig 16. Radial gas bearing design loops

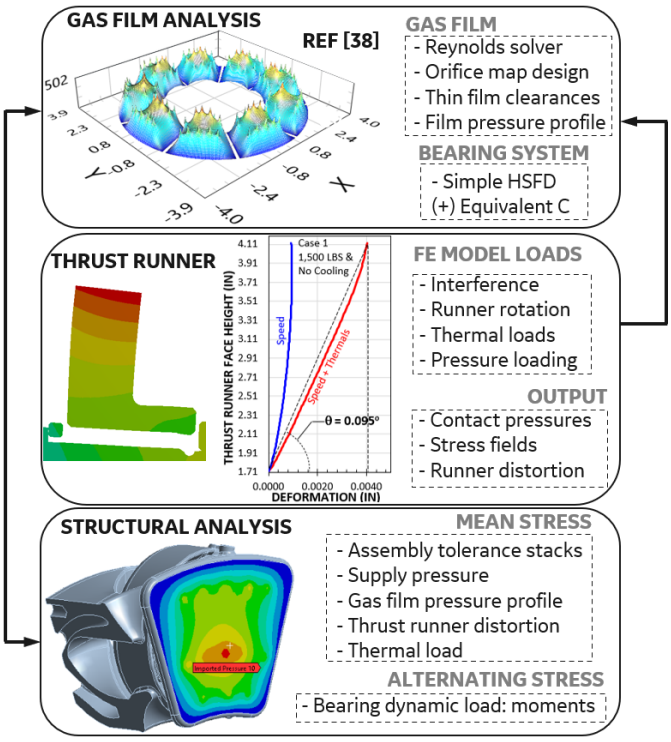

Fig 17. Thrust gas bearing design loops

High rotating surface speeds of the runner in combination with high loads can generate significant thermomechanical distortions leading to potential risks with compromised load carrying capability in the lubricating film. For this analysis step, having an accurate thermal map [24] is imperative to assess feasibility of the system. In Figure 17, the analysis shows how the thrust runner distorts due to asymmetric heating on the thrust runner. This out-of-plane misalignment needs to be absorbed by both the gas film and the structure of the bearing system. The final element of the thrust bearing design loop evaluates static and alternating stresses to assess life and reliability of the component.

6. ROTORDYNAMICS

The oil-free dual spool turbomachine concept [7] uses two separate turbomachine drivetrains for the power cycle that possess different challenges to bearing requirements and rotordynamics. From the previous study [7], the bearing requirements for the gas generator included a desired equivalent stiffness and damping magnitude for positioning critical speeds and providing adequate damping to the rotor system. Table 3 summarizes the bearing requirements for the current test rig. A two-dimensional rotordynamic FE model was created for the rotating system as shown in Figure 18. The model represents the turbo-compressor shaft coupled to the generator shaft at the spline connection. The FE model is connected to ground through three bearing elements. Figure 19 shows the synchronous rotordynamic force coefficients generated from the bearing design tool described in Figure 16, where the equivalent damping value is near 50 lb-s/in and the stiffness is approximately 100 klbs/in as required in reference [7].

Table 3. Radial bearing and drivetrain details

WORKING FLUID	CO_2
DRIVETRAIN LENGTH in (m)	53 (135)
DRIVETRAIN TOTAL WEIGHT lbs (kg)	180 (82)
BEARING DIAMETERS in (mm)	2.9 (74)
MAX BEARING SURFACE SPEED (m/s)	105
BEARING UNIT LOAD PSI (MPa)	8.4 (58) / 9.6 (66) / 4.7 (32)
BEARING K REQ. klb/in (MN/m)	100 (17.5)
BEARING C REQ. lb-s/in (kN-s/m)	50 (8.7)

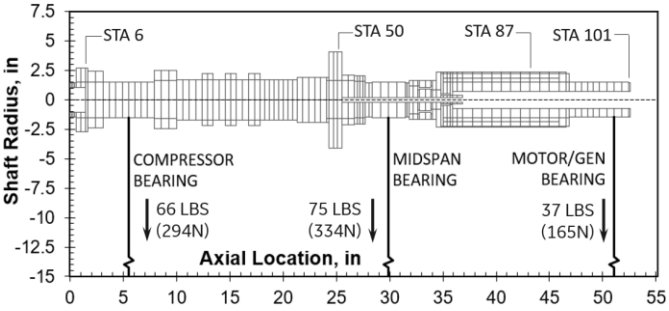

Fig 18. Lateral rotordynamic FEA model

Unbalance locations are shown in Figure 18 and represent antinodes of vibration for different rotor modes. These unbalance locations are used to assess the worst-case synchronous response for the system.

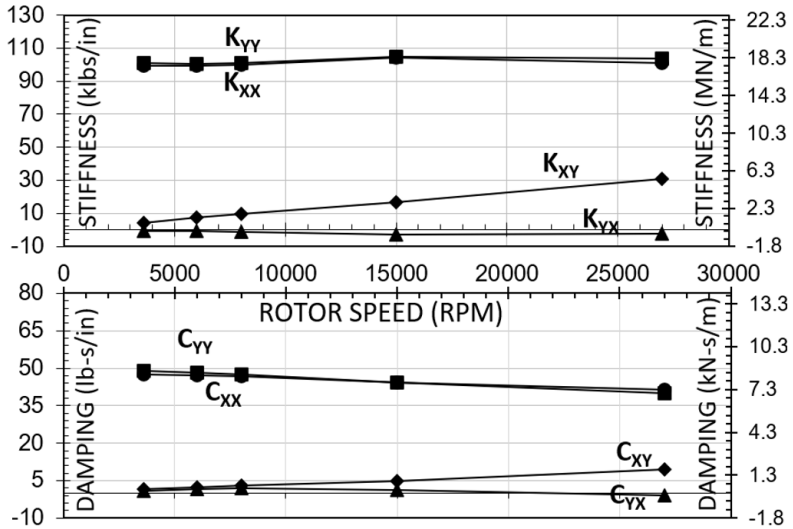

Fig 19. Midspan bearing: Equivalent direct and cross-coupled synchronous force coefficients

The first step in a rotordynamics analysis is to generate an undamped critical speed map as shown in Figure 20. The undamped critical speed (UCS) map consisted of calculating undamped rotor natural frequencies, while including gyroscopic effects for varying bearing stiffness values. This calculation is performed for the modes that need to be traversed and the first mode above the maximum continuous operating speed (MCOS). As predicted in reference [7], an

equivalent bearing stiffness of 100 klb/in results in operation between the third and fourth critical speeds. This fact requires the rotor bearing system to traverse the first bending mode (third critical speed) to achieve maximum speed and poses risks regarding film rupture from dynamic radial bearing over-loads through critical speed transitions and dynamic angular misalignment of the thrust runner.

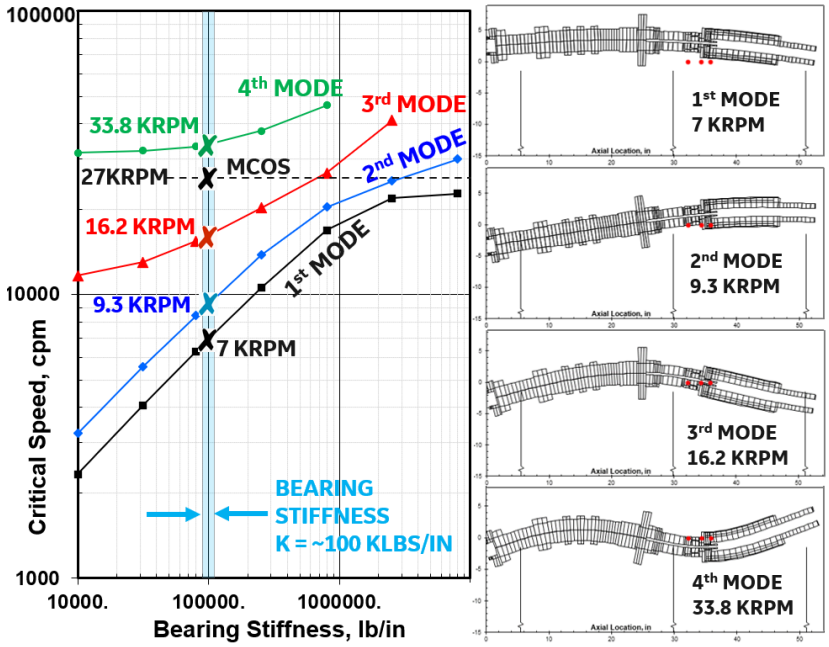

Fig 20. Undamped critical speed map

The intent of the proposed test rig concept is to evaluate these bearing risks for varying levels of rotor unbalance and to validate existing design tools for rotordynamics and bearing systems. The unbalance magnitudes used in the analysis are adopted from the American Petroleum Institute standard for rotor unbalance [40]. For multi-component rotor systems, a 12 X safety factor (multiplier) is imposed on the API 684 specification, as shown in the following equation:

$$Unbalance\ (oz-in) = 12 \cdot \frac{Rotor\ Weight\ (lbs)}{Rotor\ Speed\ (rpm)}$$

Where the unbalance is in the units of oz-in, rotor weight is in pounds, and rotor speed is in revolutions per minute (rpm). Table 4 lists the unbalance configurations applied to the rotordynamic model in Figure 18 for exciting the first 3 critical speeds.

Table 4. Rotor unbalance configurations

Unbalance Station	Amount (oz-in)	Phase (degrees)	Excited Mode	API Magnitude*
50	0.080	0	1st mode	12 X API
6	0.040	90	2nd mode	6 X API
87	0.040	270	2nd mode	6 X API
6	0.027	225	3rd mode	4 X API
50	0.027	45	3rd mode	4 X API
101	0.027	225	3rd mode	4 X API

Figures 21 and 22 illustrates the synchronous rotordynamic response results for the rotor-bearing system. The rotor vibration response and dynamic loads at bearing locations (Figure 21) reveal the three critical speed resonances located between 7-17krpm. Deflected rotor shapes for these three locations including MCOS are shown in Figure 22.

The first two modes are mainly compressor end modes whereas the third mode is a classic first bending mode. Typically, the third mode is designed out of the operating speed margin but for the current concept power density is a driving requirement for minimizing cost and maximizing efficiency. Bending modes are not only challenging to bearing systems as previously discussed but also can pose a challenge to rotor stresses and clearance closures.

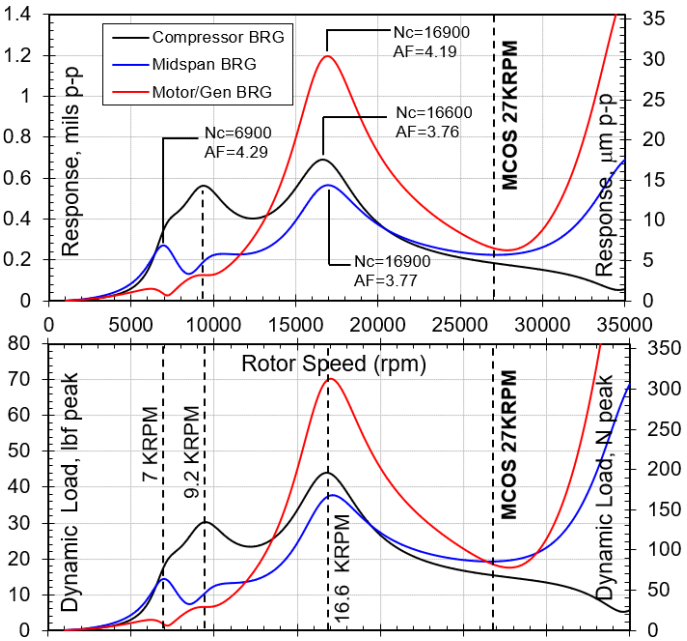

Fig 21. Synchronous response to rotating unbalance

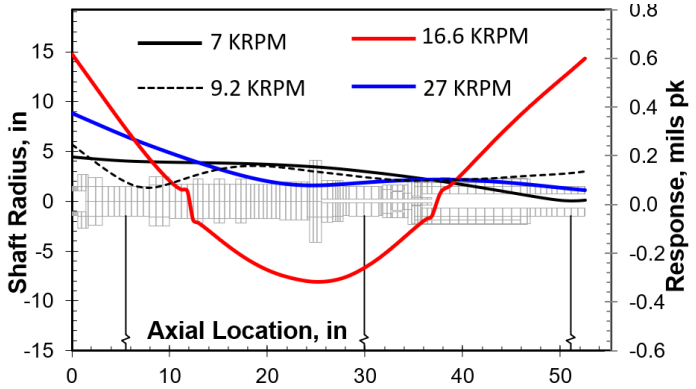

Fig 22. Deflected rotor shapes through critical speed transitions and at MCOS

This is because with a traditional 2 bearing straddle mounted rotor system the third critical speed often possesses a node of vibration at the bearing locations. The minimized motion at the bearings for the bending mode make the system suspectable to high dynamic bearing loads and rotordynamic instability at high operating speeds. To help address these risks, a three-bearing system is used in this concept and allows for more motion at bearing locations and therefore opportunity for a better damped system.

7. Thermal System Design and Analysis

This section discusses the thermal analysis model for the test rig. Specifically, as part of the thermal model, we present an ASPEN HYSYS model of the external flow loop that tracks the thermodynamic state of the CO2 gas supplied to the rig. Internal to the rig, the thermal model consists of a fluid-advection network that is thermally coupled with a steady-state thermal conduction solver to predict the windage heat, heat transfer coefficients, metal and fluid temperatures in the rig. The internal fluid advection network uses simple 1D fluid elements and real-gas CO2 properties for internal rig flows as well as commercial CFD software for modeling complex thin-film flows in gas bearings. The thermal model uses the principle of energy conservation to couple the heat flow in the advection network with the heat exchanged with the surrounding rig structural/rotating parts. The thermal model was implemented using an in-house solver using ANSYS workbench and ANSYS APDL script as the underlying platform. We present baseline temperature predictions for the test rig and quantify the amount of cooling mass flow needed to operate the test rig with its temperature constraints. We study the role of cooling in enabling reliable operation of the gas bearing system and electric machine at various rig internal pressures.

Natural gas (NG) compressor stations use small gas turbines (operating with a simple open-loop air Brayton cycle) to power NG compressors to boost pipeline pressure. The Annual Energy Outlook (AEO) for 2022 forecasts NG to be the most consumed form of energy over the next 30 years [41]. This predicted increase in demand for NG will need increased pipeline throughput—preferably at low cost and with a low emissions impact. To help meet these demands, a reference paper [42] presents a supercritical carbon dioxide (sCO2) waste heat recovery (WHR) bottoming cycle powered by the exhaust gas of an industrial 34kHP aeroderivative gas turbine. Using sCO2 as the working fluid allows for an efficient, self-contained, and remotely operable solution for this WHR unit.

In a past paper, Ertas et al. [42] present a hermetic oil-free sCO2 dual-spool power train as a concept for the sCO2 WHR unit shown in Figure 23b, which consists of a high-speed (27krpm) turbine-compressor that is aerodynamically coupled with a low-speed (12krpm) power turbine. The sCO2 WHR concept utilizes a recuperated cascaded Brayton cycle operating with 237 bara and 485 oC sCO2 on the high-pressure side and 83 bara and 35 oC sCO2 on the low-pressure side, while recovering 8.5MW of emission-free electric power from the gas turbine exhaust. Furthermore, Ertas et al. [42] present details of the high-speed turbo-compressor, also referred to as the gas generator. The cross-section of this high-speed hermetic turbo-compressor is shown in Figure 23c (taken from reference [42] and presented here for background information related to this report). The machine architecture in Figure 2c comprises of a sCO2 centrifugal compressor stage (label-1) mechanically coupled to a three-stage sCO2 turboexpander (label-2), which then couples to a 1MW direct-drive starter-generator (label-3). This hermetic machine uses three CO2-lubrciated hybrid radial gas bearings (labels-4,5,6) and one thrust bearing (label-7) to support the rotor assembly. Unlike traditional gas foil bearings that operate with hydrodynamic gas films, hybrid gas bearings [43] use a combination of hydrodynamics and pressurized hydrostatic CO2 to create a load-bearing fluid film. Moreover, implementing such hybrid bearings in 10-MW-scale turbomachinery needs development of damper technology [44] to provide adequate amount of rotordynamic damping. A film-riding seal [45-46], shown with label-8, isolates the starter-generator cavity and the bearings housed in this cavity from the high-temperature turbine exhaust. Figure 23d shows a simplified rotor to simulate the drivetrain system in an experimental rig. Such a hermetic turbomachinery configuration (only the high-speed configuration is discussed here, see reference [42] for the low-speed turbomachine) can eliminate 600-800 metric tons of CO2 leakage annual emissions compared to conventional 10-MW-class sCO2 turbomachinery [47-49] that typically employs at least 4 dry gas seals in shaft end locations. Furthermore, such architectures enable the removal of high-cost items like the lubrication skid and power transmission gearbox.

The high-speed hermetic turbo-compressor with a starter-generator shown in Figure 23c has several critical risks that need to be mitigated with full-scale experimental demonstration/testing. These risks include (a) characterization of rotordynamic performance up to 27krpm with a rotor fully supported on hybrid gas bearings [43,44], (b) benchmarking of additively manufactured gas bearings with dampers [44], (c) thermal characterization of the system in a high-pressure immersed CO2 environment.

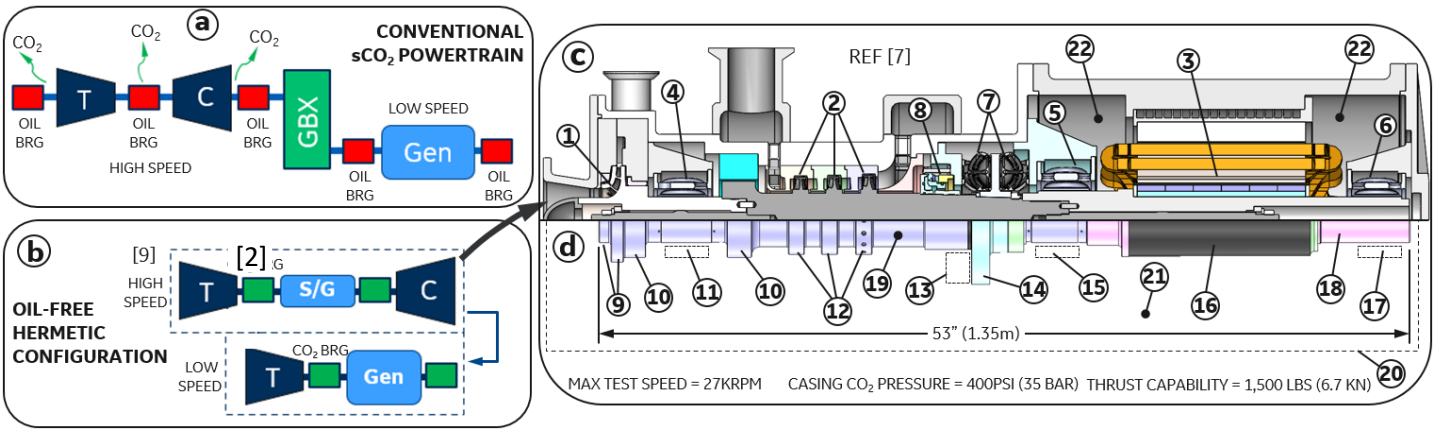

FIGURE 23. Oil-free drivetrain and test rig rotor concepts: (a) conventional sCO_2 power train, (b) dual-spool oil-free hermetic power system [2], (c) conceptual design of high-speed gas generator for a sCO_2 WHR unit [2], (d) simplified test rotor for reducing risk. (1) 3.87MW centrifugal compressor, (2) 4.83MW 3-stage turbine, (3) 1MW starter-generator, (4) compressor -end radial bearing, (5) mid-span bearing, (6) generator-end bearing, (7) thrust bearings, (8) film-riding seal, (9) rotor-steps simulating the centrifugal impeller inertia, (10) balance piston, (11) compressor bearing location, (12) rotor-steps simulating turbine, (13) thrust bearing location, (15) midspan radial bearing location, (16) 1MW starter-generator, (17) generator-end radial bearing location, (18) permanent magnet electric machine shaft, (19) turbo-compressor shaft, (20) hermetic CO_2 pressure boundary, (21) 400psi CO_2 environment, (22) electric machine cavity

A past paper [50] presents an equivalent test rig rotor system design – engineered to experimentally test and address the critical risks listed above. A cross-section of the test rig, as presented in the a previous paper [50], is shown here in Figure 24. High-pressure CO2 is supplied to this test rig with an external flow loop that includes gas boosters, regulators, flow meters and chillers for a steady state operation. Details of this test rig and flow loop will be described in Section 7.0. The test rig will use novel additively manufactured externally pressurized gas bearings while having the capability to apply thrust, assess rotordynamics, and benchmark thermal models. The main objective of the present thermal section is to develop a thermal prediction model of this test rig and flow loop to evaluate the cooling flows required for reliable operation of the CO2-immersed electric machine as well as the CO2-immersed gas bearings.

Miller et al. [51] performed tests with a 25krpm motor-generator (6.93-inch or 17.6 cm diameter) operating in an immersed CO2 environment (7bar, 50oC). Miller et al. [51] used CO2 circulating internally through the rotor-stator gap as well as water circulating through a water jacket around the motor housing for cooling the motor generator. Miller et al. [51] also present thermal modeling along with the test data. Compared to Miller et al. [51], the CO2-immersed motor/generator presented in the present report is slightly smaller (~4.82-inch or 12.24 cm diameter), about the same speed (27krpm) but possesses a higher operating pressure (27.6 bara, 50oC-100oC) resulting in higher aerodynamic windage losses. Similar cooling schemes of rotor-stator gap cooling and water-jacket-based cooling are studied in the present work. Furthermore, the present work also studies CO2-immersed gas bearings and the cooling flows needed to operate such bearings reliably when large windage heating is expected due to the high-pressure environment.

Alban et al. [52] advanced a hermetic electric motor driven centrifugal compressor system operating at 12krpm, with a suction pressure of 50 bar. Cooling flow was extracted from the first impeller exit and throttled to cool the immersed electric motor and 4 active magnetic bearings. Alban et al. [52] note that the cooling flow needed for the immersed electric motor was one order of magnitude higher than that needed for the magnetic bearings; and overall meant that the first stage impeller needed to be oversized 5-15% to accommodate the cooling needed for the magnetic bearings and motor. While the thermal/cooling scheme from Alban et al. [52] cannot be quantitively compared with the present report, the work of Alban et al. [52] is very similar to the present report in its approach of using non-oil-lubricated bearings for MW-class machines and an electric machine operating in a high-pressure immersed environment.

Several recent 10 MW-scale sCO2 turbomachinery [47-49,53] have reported thermal analyses work performed in course of assessing the thermal loads on the turbomachinery. Specifically, the SunShot sCO2 turbine [53] and the STEP sCO2 turbine [47] have used thermal models to assess casing and rotor thermal loads for thermal stresses and creep analyses. Such barrel-type turbines [47,53] and the integrally geared compressor-expander [49] package low- to medium-temperature-limited components (e.g., Dry Gas Seals with a temperature rating ~190oC) in the vicinity of a 700oC high-temperature turbine – that invariably needs detailed thermal analyses to understand the heat transfer and ensure that temperature limits or stress limits for various closely-packaged components are not exceeded.

The high-speed, hermetic test rig [50] in the present work (see Figure 3) needs a detailed thermal analysis to (a) predict temperatures and ensure temperature-limited parts (e.g., carbon sleeve of motor rotor, glued laminates of motor stator) are sufficiently cooled, (b) ensure sufficient heat removal in gas bearings to avoid thermal distortions in thin-film clearances, (c) predict thermal loads needed to calculate thermal clearance closures of labyrinth seals, loss of collinearity of radial bearings, and (d) provide thermal loads necessary for analyzing thermal stresses of various subcomponents. With these objectives in mind, this report develops a three-dimensional (3D) thermal model for the test rig [50] of Figure 24. The thermal model accounts for the heat transfer between the structural subcomponents shown in Figure 24 with the CO2 flowing through the test rig. Note that the CO2 supplied to this test rig circulates through a closed-loop flow circuit involving gas boosters, chillers and pressure regulators that are also described in this report.

The remainder of this report is arranged in the following fashion. Section 7.0 briefly describes the experimental test rig of Figure 24 and the CO2 flow loop used for circulating CO2 to this rig. Section 3.0 describes the thermal model for internal heat transfer of the rig and an ASPEN HYSYS model for the thermodynamic CO2 flow-loop modeling. Section 9.0 discusses the thermal prediction results for the test rig along with various scenarios analyzing the cooling flows.

8. TEST RIG AND FLOW LOOP

This section describes the test rig (subsection 7.1) and the associated Gas Supply Flow Loop (subsection 7.2).

8.1 Test Rig

The test rig cross-section is shown in Figure 24. The test rig simulates the turbo-compressor with stater-generator (of Figure 23c), except the compressor impeller and the 3-stage turbine are simulated with equivalent rotating inertia disks. The rotor assembly is supported with three additively manufactured radial gas bearings and one additively manufactured thrust gas bearing, which are all housed inside a hermetic casing. The test rig is filled with high-pressure CO2 supplied from the Gas Supply Flow Loop. A pair of labyrinth seals (near the center section) form a thrust chamber, which when pressurized pushes the thrust collar leftwards. This axial thrust applied on the thrust collar is supported by the thrust bearing. A 300-kW permanent magnet motor is used to drive this rig to 27 krpm with the motor immersed inside the hermetic chamber. The rotating permanent magnets are supported by a thin rotating carbon sleeve. The motor stator is wrapped in a water jacket for heat removal. A magnetic gap cooling plenum and magnetic gap cooling conduits are used to direct CO2 cooling flow between the rotating carbon sleeve and stationary motor windings i.e. the magnetic gap.

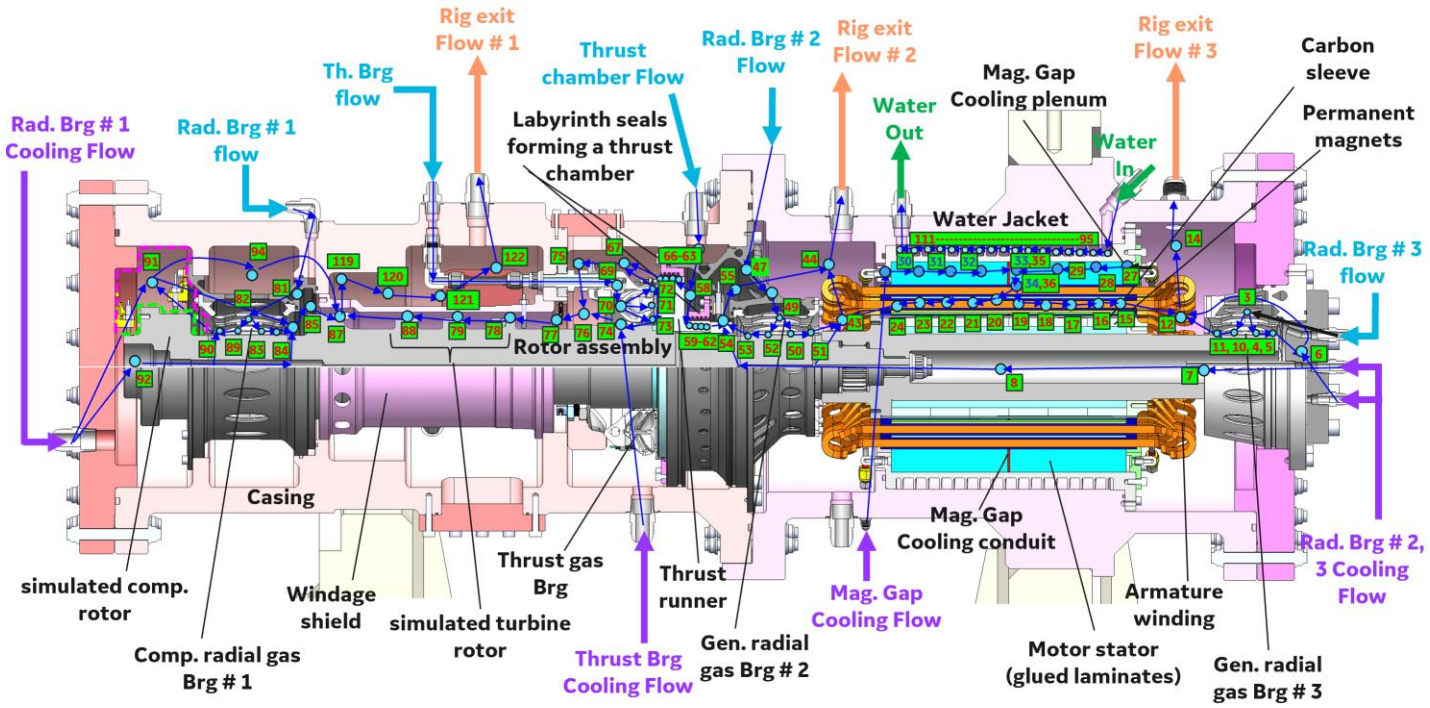

FIGURE 24. Test rig cross-section showing internal CO_2 flow advection network, CO_2 flow inlets and outlets, and water flow inlet and outlet

The casing has several CO_2 inlets—five inlets shown in cyan color labels represent the external pressurization flow for each of the 4 bearings and the flow required to pressurize the thrust chamber. Furthermore, 5 inlets shown in purple color labels represent locations for introducing additional CO_2 cooling flow for the bearings and the motor magnetic gap. The green color labels represent the cooling water inlet and exit. Finally, the three orange labels show three CO_2 exit locations for removing the CO_2 heated inside the rig. Internal to the test rig, there is a network of blue dots and blue arrows, which will be described in Section 8.

8.2 Gas Supply Flow Loop

The Gas Supply Flow Loop (GSFL) is a closed CO_2 flow loop that will maintain the test casing internal pressure at 400 psia (27.6 bara), while supplying higher-pressure CO_2 to the three radial gas bearings, support 1500 lbs of thrust by the novel gas thrust bearing, pressurize the thrust chamber to create the thrust, and provide cooling flow to remove windage heat. The GSFL is a separate stand-alone skid controlled by a GE designed control system but with on-board control capability to shut down the test system safely when necessary. The piping diagram and flow circuit layout is shown in Figure 25.

The GSFL consists of the following components. High-pressure CO_2 tanks are used to charge the system and the Supply Tank with CO_2 and sustain CO_2 mass flow in the system during the test. Supply Tank pressure will be maintained near 363 psia (25 bara) during the test. A single high pressure gas booster (HPGB) and seven low pressure gas boosters (LPGB) are used to raise the pressure of the CO_2 in the Supply Tank to levels sufficient to drive the necessary CO_2 mass flows through the thrust bearing and radial bearings during the testing. The gas boosters are activated by 130 psig compressed air (sourced from building compressed air supply line) and will operate at 50 cycles per minute. HPGB outlet pressure will range from 954-1012 psia (about 66-70 bara). LPGB outlet pressure will range from 663-727 psia (about 46-50 bara). The heat of compression will be removed by water-cooled shell and tube heat exchangers. The HP Cooler outlet temperature is 55 ^oC while the LP Cooler outlet temperature is 40 ^oC. Buffer tanks are employed to reduce pressure oscillations. The HP manifold supplies gas to the thrust bearing feed line while the LP manifold distributes gas to the radial bearing line, the thrust chamber line, the EM gap cooling line and the Mass Flow Cooling line. Each gas line has a pressure reducing pressure regulator which will set the pressure in the line to the test casing, and a Coriolis flow meter to measure the flow in the line. Each pressure regulator will employ a micro-processor based, electropneumatic PID controller. These controllers allow the control system to remotely control gas inlet pressures to the test components. Using these controllers, it is possible to remotely vary radial and thrust bearing mass flows, vary thrust from 250-1500 lbs., while making adjustments to cooling flows. The GSFL will receive a single gas return line from the test casing, passing

the flow through a water-cooled shell and tube heat exchanger, labeled as the Return Cooler. The Return Cooler is designed to deliver 35 °C gas at its outlet. Between the Return Cooler and the Supply Tank, there is a back-pressure pressure regulator (PRRF) as well as a Coriolis flow meter. PRRF also has an electropneumatic controller and will be used to maintain the pressure upstream in the test casing at 400 psia (27.6 bara).

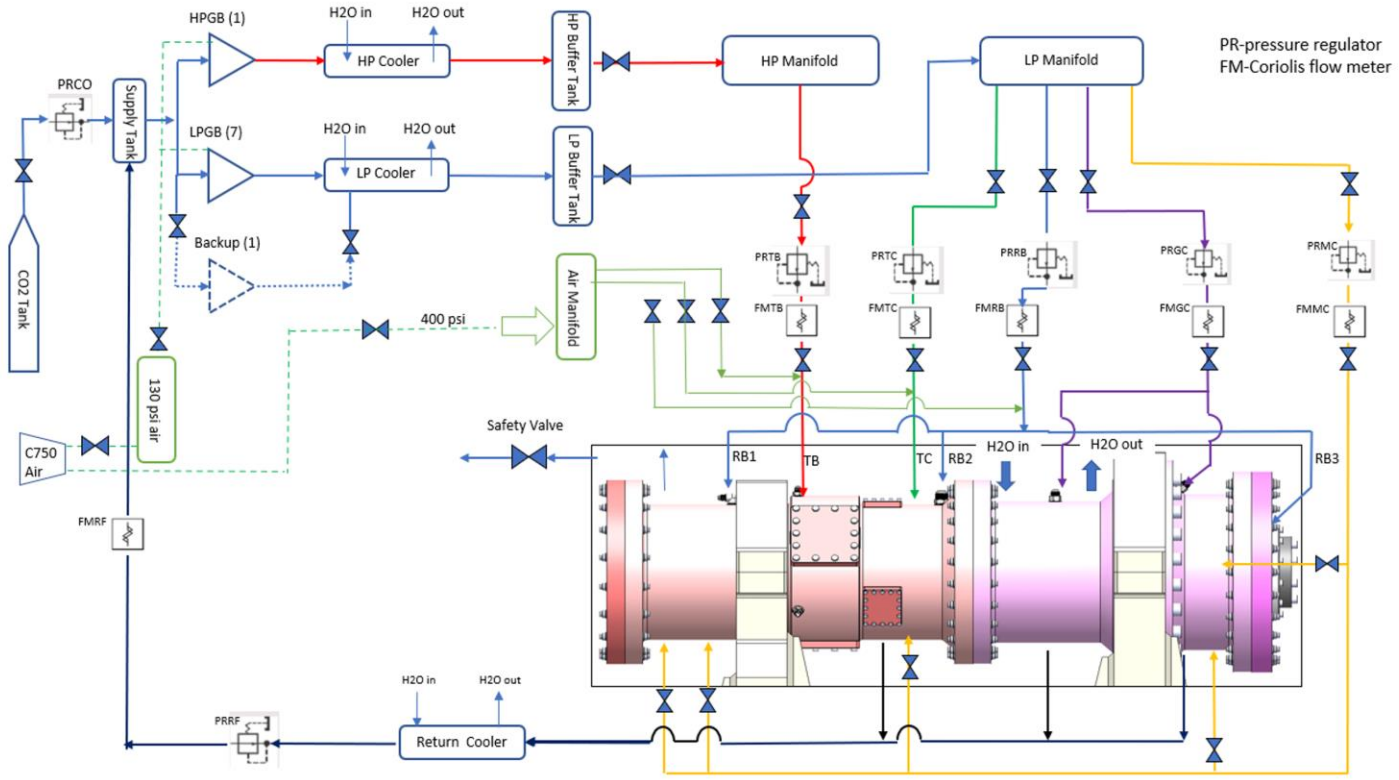

FIGURE 25. Gas Supply Flow Loop HP- high pressure, LP – low pressure, EM – electric machines, TB – Thrust Bearing, RB1 – Radial Brg. # 1, RB2 – Radial Brg. # 2, RB3 – Radial Brg. # 3, TC – Thrust Chamber, HPGB – High Pressure Gas Booster, LPGB – Low Pressure Gas Booster, PRCO – Pressure Regulator CO_2, PRTB – Pressure Regulator Thrust Brg, PRRB- Pressure Regulator Radial Brg, PRTC – Pressure Regulator Thrust Chamber, PRGC – Pressure Regulator EM Gap Cooling, PRMC – Pressure Regulator Mass Flow Cooling, PRRF – Pressure Regulator Return Flow, FMGC – Flowmeter EM Gap Cooling, FMMC – Flowmeter Mass Flow Cooling, FMRF – Flow meter Return Flow

9. THERMODYNAMIC AND THERMAL MODELING

This section describes the test rig internal heat transfer model (subsection 8.1) and gas flow loop thermodynamic model (subsection 8.2).

9.1 Thermal model for heat transfer inside the test rig

The test rig internal heat transfer model was set-up using an in-house iterative solver. As shown in Figure 26, separated by the vertical dashed line, the in-house solver has two modules - (a) a structural thermal solution module implemented using ANSYS Workbench, and (b) an advection network solution module implemented using an ANSYS APDL script.

The advection flow network for the test rig is shown with blue circles and blue arrows in Figure 24. For this test rig, the advection flow network comprised of 110 internal nodes (numbers shown in green squares next to each blue dot in Figure 24, some numbers are omitted for clarity). Each blue dot represents a fluid node that is associated with a control volume around it. For example, node 91 (top left of Figure 24) is associated with an axisymmetric control volume enclosed by the magenta dashed line (stator area tied to fluid node 91) and green dashed line (rotor area tied to fluid node 91). Some fluid nodes are associated with rotating cavities (e.g., node 91, node 84, node 78, node 43, node 15 etc.), while some others are tied to stationary duct type flows (e.g., node 30, node 31, node 34 etc.). Each of the three radial bearings was assigned four rotating cavity fluid nodes, while the thrust bearing was assigned three rotating cavity nodes. The motor magnetic gap was divided into 10 rotating cavities with each one assigned a fluid node, and each tooth pocket of the labyrinth seal was assigned one fluid node. Each blue arrow inside the rig represents transport of enthalpy from one fluid node to the next as the working fluid traverses the test rig flow circuit.

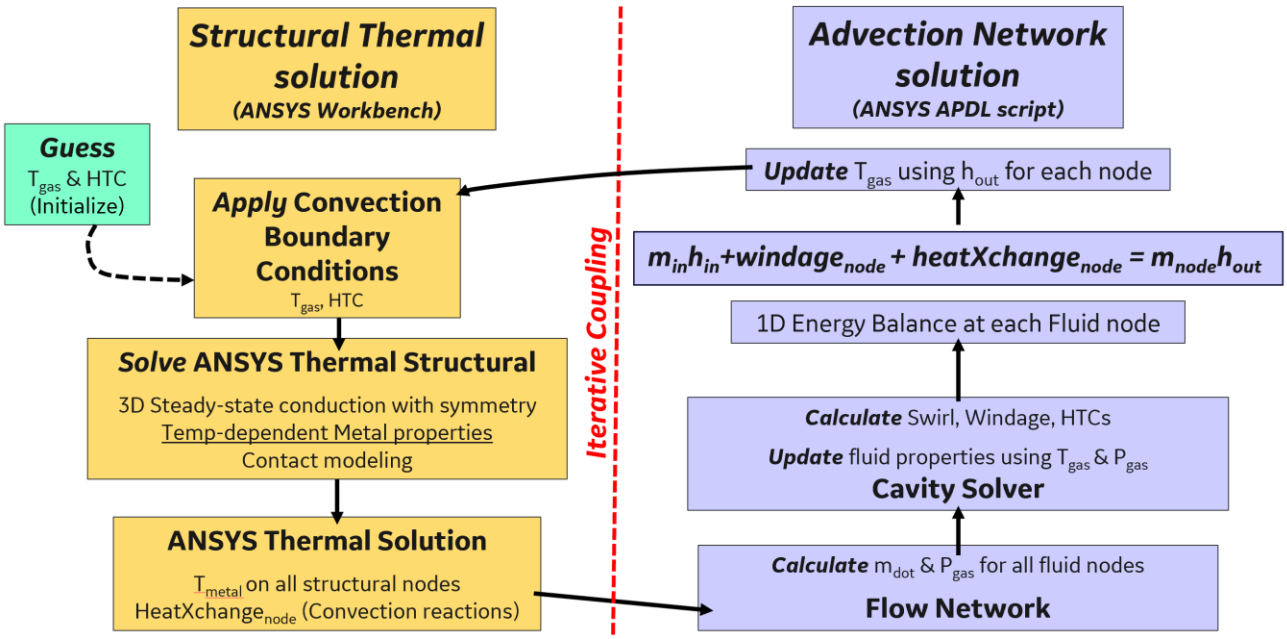

FIGURE 26: Overview of In-house Thermal Solver

A first step in setting up the advection network is the fluid flow solution (see bottom right of Figure 26). In this first step, the flow between each connected fluid node on the network is modeled using 1D fluid resistance elements (e.g.,

pipe flow element, orifice flow element with real gas CO_2 properties) to solve and assign a mass flow m_{dot} to each arrow. This flow network solution was implemented using a MATLAB-based script. Since the fluid flow resistance models are more complicated in the cases of fluid nodes tied to the gas bearing films (e.g., fluid nodes 71, 72, 73, 4, 5, 10, 11 etc.), ANSYS CFX was directly used to calculate the bearing fluid flow (the CFX models are described in a reference paper Ertas et al. [42]). The flow across the two labyrinth seals was calculated using GE proprietary solvers (airflow based) and adjusted for the properties of CO_2. The correctness of these labyrinth seal calculations was verified with ANSYS CFX models (using CO_2 real gas properties). The two methods for calculating the labyrinth seal flow are in agreement with one another within 10%.

For each fluid node tied to a rotating cavity, we compute an associated swirl (fluid tangential motion) using stator area drag, rotor area windage, and conservation of angular momentum of the fluid received from its upstream fluid node. Accurate swirl values are needed for estimating aerodynamic windage heat produced in that cavity. For all rotating cavities, the solver uses GE proprietary turbulent windage correlations for computing windage, except the gas bearing film nodes. The ANSYS CFX models of the gas bearings [42] showed windage being higher than the ones predicted by GE proprietary turbulent windage correlations. Consequently, the bearing film nodes were assigned higher windages consistent with the CFX models, which is the conservative design approach to be verified experimentally. For every fluid node (rotating cavity or not), the local fluid velocity and fluid properties (density, dynamic viscosity, conductivity, heat capacity) are used to compute Reynolds number, Prandtl number – which are then combined with GE proprietary correlations to obtain the Nusselt number and heat transfer coefficients (HTCs).

The next step is to create the structural thermal model using ANSYS Workbench. A quarter 3D geometry of the rig is used with symmetrical boundary conditions to reduce the computational effort. Temperature-dependent material properties are assigned to the geometry. The contacts between each of the components are set up in ANSYS Workbench and the geometry is meshed with tetrahedral elements. The surfaces associated with each of the cavity nodes are selected and named. These surfaces are pointers to apply HTCs and gas temperatures (T_{gas}). For example, fluid node 91 will exchange heat with the green-dashed and magenta-dashed areas shown in Figure 24.

The iterative scheme is outlined in Figure 26. The iteration commences (on the left side of Figure 26) with initial guesses for HTCs and T_{gas} at each fluid node. Using these, the convection boundary conditions are applied to the structural solver, which is solved in steady state to obtain structural temperature T_{metal} and the heatXchange convection reactions for each fluid node. At this point, the solver hands-off to the advection network module. The fluid node temperatures T_{gas} and pressure P_{gas} are used to update the fluid properties, which are then used to compute HTCs using GE proprietary correlations. The swirl and windage for each node are also updated using the latest T_{gas} and P_{gas}. For each fluid node (say node X), a conservation of energy constraint is imposed for the control volume around fluid node X. This is shown in Equation (1) below:

$$\sum m_{in}h_{in} + \text{windage}_{node\ X} + heatXchange_{node\ X} = m_{out}h_{out} \quad \ldots(1)$$

where, $\mathbf{\sum m_{in}h_{in}}$ represents summation of incoming fluid enthalpies from all nodes that are upstream of fluid node X, '$\mathbf{windage_{node\ X}}$' represents the calculated windage (during the latest iteration) for the cavity around node X, '$\mathbf{heatXchange_{node\ X}}$' represents the convection reaction computed by ANSYS in the previous iteration for the areas tied

to fluid node X, and '$\mathbf{m_{out}h_{out}}$' represents the outgoing enthalpy for this cavity node X. In this equation, all items are known except $\mathbf{h_{out}}$. After calculating $\mathbf{h_{out}}$, we can use it to calculate a new T_{gas} for the fluid leaving node X, before proceeding to solve Equation (1) for the next fluid node. Once the T_{gas} for all fluid nodes are updated, the iterative solver hands the solution back to the structural side (see Figure 26) where the next iteration of the structural thermal solution commences with the recently solved T_{gas} and HTCs. This process continues until T_{metal} and T_{gas} converge to withing 0.5 deg F.

Note that natural convection heat transfer was imposed on the external walls of the casing, which results in very small amount of heat flow leaving through the casing. Also note that the electrical losses of the electric machine were modeled as a body load (per unit volume heat generation in the stator armature, windings and permanent magnets). The heat generation in the motor stator was based on electromagnetic FEA performed by the electric machine team as presented in the reference paper [50].

The outcome of this iterative thermal solution is the predicted metal and gas temperatures at all the fluid nodes as well as the structural mesh nodes. Additionally, we also obtain the aerodynamic windage calculations, HTCs, and swirl at the fluid nodes. The solver also performs a test-rig-level energy balance check to ensure that the sum of (a) change in enthalpy of the overall CO_2 entering and leaving the test rig, (b) the change in enthalpy of the cooling water, and (c) heat lost to natural convection matches with the amount of heat generated by windage and the electrical losses.

The internal heat transfer model for the test rig described above uses the various m_{dot} entering the test rig (bearing pressurization flow, thrust chamber flow, electric machine gap cooling flow, additional cooling flow) along with their incoming temperatures as boundary conditions or inputs to the solver. Similarly, this model predicts the temperature of the fluid leaving the test rig. Of course, we need a good prediction tool to understand how the CO_2 temperature changes outside the rig as it loops through gas boosters, regulators, chillers etc. This predictive capability is obtained through the HYSYS model described in the next subsection 8.2.

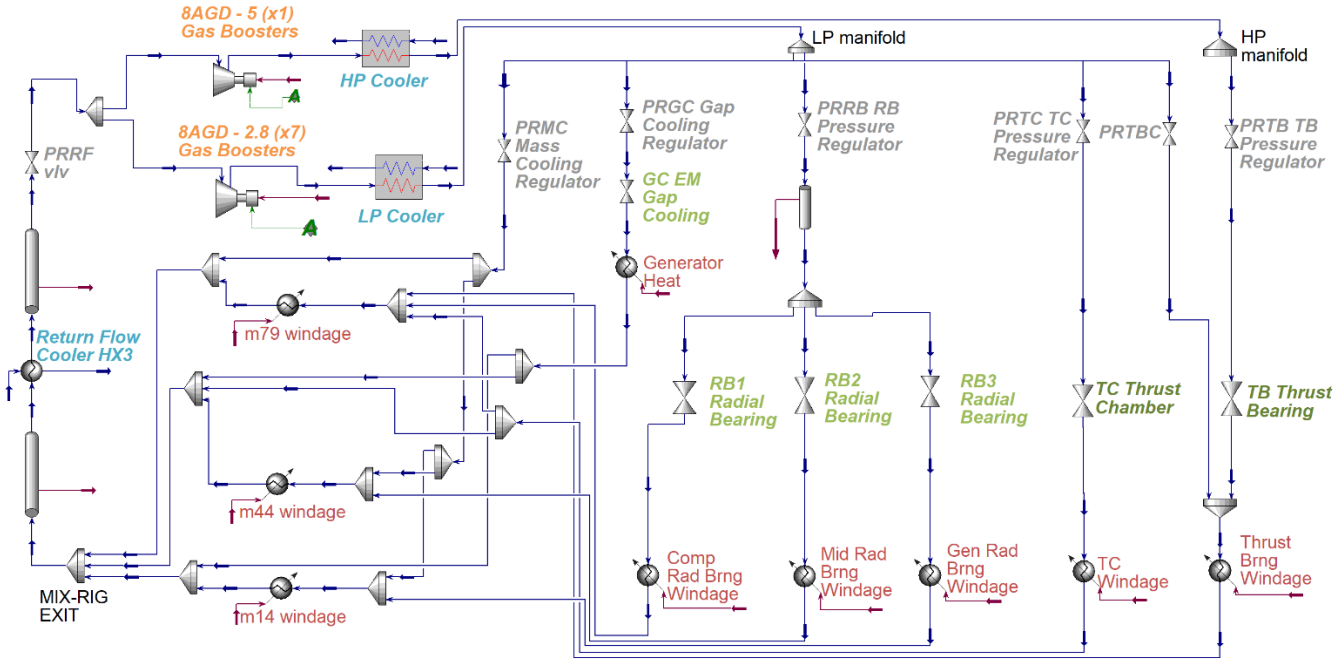

FIGURE 27: Overview of HYSYS Model for the GSFL

9.2 Thermodynamic model for flow external to the test rig

Aspen HYSYS was used to model the CO_2 Gas Supply Flow Loop (GSFL). The HYSYS model has three benefits. First, it provides accurate information about the various state points throughout the flow loop (for e.g., predictions of the gas temperatures exiting the pressure regulators). Second, it provides the capability to change test parameters and predict how the GSFL system will react during the test. Third, the HYSYS model can be used to understand the effect of certain fault conditions on the ability to successfully complete testing.

The HYSYS model consists of three sections – the Gas Booster Section, the Valve & Bearing Section, and the Test Rig Section. This model is shown in Figure 27.

The Gas booster Section consists of the Supply Tank, the high pressure (HP) gas booster, HP Cooler and HP Buffer Tank and the low pressure (LP) Gas Boosters, the LP Cooler and the LP Buffer tank. For a given supply pressure, the volumetric flow rate of a specific gas booster is determined by the drive air pressure and the pressure increase across the gas booster. Using software provided by the Gas booster vendor, transfer functions for volumetric flow rate were established for a range of supply and outlet pressures and were programmed into the HYSYS model. This enabled the HYSYS model to calculate the gas booster flow rate and cycles per minute as a function of pressure increase across the gas booster. The coolers are modeled as simple shell and tube heat exchangers.

The Valve & Bearing Section consists of the HP and LP gas delivery systems. The HP gas system consists of a single gas line comprising of – a flow splitter modeling the HP manifold, a valve modeling the pressure reducing regulator (PRTB), a valve modeling the thrust bearing (TB), and a heat generation element that simulates the windage heat of the thrust

bearing. The LP gas system consists of a flow splitter modeling the LP manifold, which feeds five parallel gas lines to the test rig – the radial bearing (RB) line further split into three radial bearing lines RB1, RB2, RB3, the thrust chamber (TC) line, the mass cooling (MC) line, the electric machine gap cooling (EMGC) line and a fifth line designated as the TBC line. Each of these lines have a pressure reducing regulator in series with a valve modeling the flow element followed by a heating element to simulate the windage heat produced by the respective element. For example, the thrust chamber line consists of a valve modeling the pressure reducing regulator (PRTC), in series with a valve modeling the TC, and a heat generation element that simulates the windage heat produced in the TC.

The Test Rig Section consists of a number of Mixers, the Return Cooler and the back-pressure regulator (PRRF) that is controlling the pressure in the test casing constant at 400 psia. The Mixers simulate how various gas flows mix together internal to the test rig before exiting through the Rig Exit Flow lines #1, 2 and 3 depicted in Figure 24. Each Mixer conducts an energy balance that is used to predict the resulting temperature. Rig Exit Flows #1, 2 and 3 pass through a final Mixer that feeds the Return Cooler. The Return Cooler is modeled as a shell and tube heat exchanger. The Return Cooler lowers the gas temperature from the Test Rig exit to 35 ^{o}C and delivers it to PRRF, modeled as a valve. PRRF delivers cool gas at approximately 363 psia to the Gas Booster Supply Tank, closing the Flow Loop.

The HYSYS Flow Loop calculation begins in the Valve & Bearing Section. The user inputs thrust force and gas pressure values entering the Test Rig for the lines TB, RB1, RB2, RB3, MC and EC. The user also inputs cooling mass flow rates desired for lines MC and EMGC. The HYSYS model calculates the mass flow, film thickness and windage heat at each bearing based on the input pressure using transfer functions derived from separate CFD calculations presented in a past paper [42]. The input thrust force is used to calculate the pressure acting on the thrust chamber surface area. This pressure is then used to calculate the mass flow leaking though two labyrinth seals using a transfer function. This establishes the mass flow rate in line TC. The TBC line mass flow is the LP Gas Booster maximum flow capacity minus the flows in lines RB, TC, MC and EMGC.

At this point all the mass flow rates and pressures at the Test Rig are known but the gas pressures upstream of the pressure regulators back to the Gas Boosters are not. The HYSYS Model exports all the gas mass flow rates to the Gas Booster Section. The Gas Booster Section determines the total mass flow rate required for the HP and LP Gas Boosters. Using the Gas Booster transfer functions described above and an Adjust feature in HYSYS, this section iterates on Gas Booster pressure increase until the flow rate result converges on the total flow determined by the Valve & Bearing Section. With a converged solution, the mass flow rate, gas pressures and temperatures are known throughout the Flow Loop.

10.THERMAL RESULTS AND DISCUSSION

In this section, we will discuss the cooling flow and thermal results, for 7 cases:

- Case # 1: Baseline flows with rig operating at 400 psia
- Case # 2: Baseline plus thrust bearing cooling
- Case # 3: Baseline minus EM gap cooling

- Case # 4: Case # 3 minus water jacket cooling.
- Case # 5: Rig operating at 15 psia with minimal cooling
- Case # 6: Rig operating at 15 psia with some cooling
- Case # 7: Rig operating at 200 psia with some cooling

The first four cases are with the internal rig pressure set to 400 psia (27.6 bara), Case # 5 and Case # 6 are for the rig operating with 15 psia (~1 bara), and Case # 7 is with the rig operating at an intermediate 200 psia (13.8 bara). Temperature data presented for the first four cases will provide the reader insight into the role of cooling flows for enabling test rig operation with the gas bearings and the electric machine operating in an immersed 400 psia high-pressure CO_2 environment. Cases # 5, # 6 and # 7 will provide insight into reduced cooling flow requirements when the gas bearings and the electric machine operate in low pressure environments (i.e., with lower windage heating).

For the first four cases, the CO_2 pressure inside the test rig is set to 400 psia (27.6 bar). This pressure for the generator cavity (and overall test rig internal cavity) is based on the seal leakage versus windage penalty trade-off analysis for the high-speed turbomachine as presented in Ertas et al. [42]. The CO_2 flow inside the test rig is mainly a function of the pressures and the thrust load applied in the thrust chamber, which for all seven cases is set to 1500 lbf (~6675 N) axial thrust load. Applying this thrust load requires the thrust chamber pressure to be 38 psi (2.62 bar) higher than the overall test rig pressure. This higher pressure inside the thrust chamber sets the flow past the two labyrinth seals, which is the most dominant cooling flow inside the rig. However, as the results will show, cooling flows targeted around gas bearings and the electric machine are still needed to keep the temperatures at acceptable levels.

The CO_2 flow entering the test rig ranges in temperature from 18 ^oC to 40 ^oC (see Table 5) depending on how the flow gets throttled in the GSFL prior to entering the rig. The eight boosters have a total mass flow capacity of about 0.8 kg/s. The total CO_2 flow entering the rig for each of the seven cases is listed in Table 5 along with the internal pressure set in the rig. Table 5 also provides a % breakdown of the CO_2 mass flow entering the rig through various inputs. The thrust chamber labyrinth seal flow is the dominant flow (41% to 70% of the rig flow), EM gap cooling and Radial Bearing # 1 cooling flows are both the second most dominant flows (about 4% to 18% each). The gas bearing pressurization flows (to support axial and radial loads of the rotor) comprise 15% to 20% of the rig flow. The Radial Brg. # 2 and # 3 cooling flows are a small portion (4 to 6%) of the overall flow.

TABLE 5 Summary of CO_2 and water flows removing heat from the test rig for the seven cases presented. Temps of flow entering the rig and test rig internal pressures are also listed

	Flow Temp Entering Rig (°C)	Case # 1	Case # 2	Case # 3	Case # 4	Case # 5	Case # 6	Case # 7
		Baseline	Thrust Brg. ID Cooling	Remove Gap Cooling	Remove Gap Cooling & Water Flow	Atm. Pressure, No Gap cooling, No Brg. Cooling	Atm. Pressure, Some Gap & Brg. Cooling	Medium Pressure, Some Gap & Brg. Cooling
		CO_2 Flow 0.65 kg/s	**CO_2 Flow 0.76 kg/s**	**CO_2 Flow 0.54 kg/s**	**CO_2 Flow 0.54 kg/s**	**CO_2 Flow 0.104 kg/s**	**CO_2 Flow 0.14 kg/s**	**CO_2 Flow 0.37 kg/s**
		400 psia	**400 psia**	**400 psia**	**400 psia**	**15 psia**	**15 psia**	**200 psia**
Water Flow gal/min	29.44	1.4	1.4	1.4	0	1.4	1.4	1.4
Thrust Chamber kg/s (% rig flow)	21	0.31 (48%)	0.31 (41%)	0.31 (57%)	0.31 (57%)	0.073 (70%)	0.073 (51%)	0.19 (52%)
Gap Cooling kg/s (% rig flow)	18.3	0.10 (16%)	0.10 (14%)	0 (0%)	0 (0%)	0 (0%)	0.006 (4.4%)	0.048 (13%)
3 Radial Brg kg/s (% rig flow)	29 to 29.3	0.073 (11%)	0.073 (10%)	0.073 (13%)	0.073 (13%)	0.009 (9%)	0.009 (6.5%)	0.024 (6.5%)
Thrust Brg kg/s (% rig flow)	40	0.031 (5%)	0.031 (4%)	0.031 (6%)	0.031 (6%)	0.022 (21%)	0.022 (15.4%)	0.014 (3.9%)
Rad. Brg # 1 Cooling Flow kg/s (% rig flow)	18	0.1 (15%)	0.1 (13%)	0.1 (18%)	0.1 (18%)	0 (0%)	0.025 (17.4%)	0.07 (18.9%)
Rad. Brg # 2, 3 Cooling Flow kg/s (% rig flow)	18	0.03 (4%)	0.03 (4%)	0.03 (6%)	0.03 (6%)	0 (0%)	0.0075 (5.3%)	0.022 (5.8%)
Thrust Brg. ID Cooling kg/s (% rig flow)	18	0 (0%)	0.113 (15%)	0 (0%)	0 (0%)	0 (0%)	0 (0%)	0 (0%)

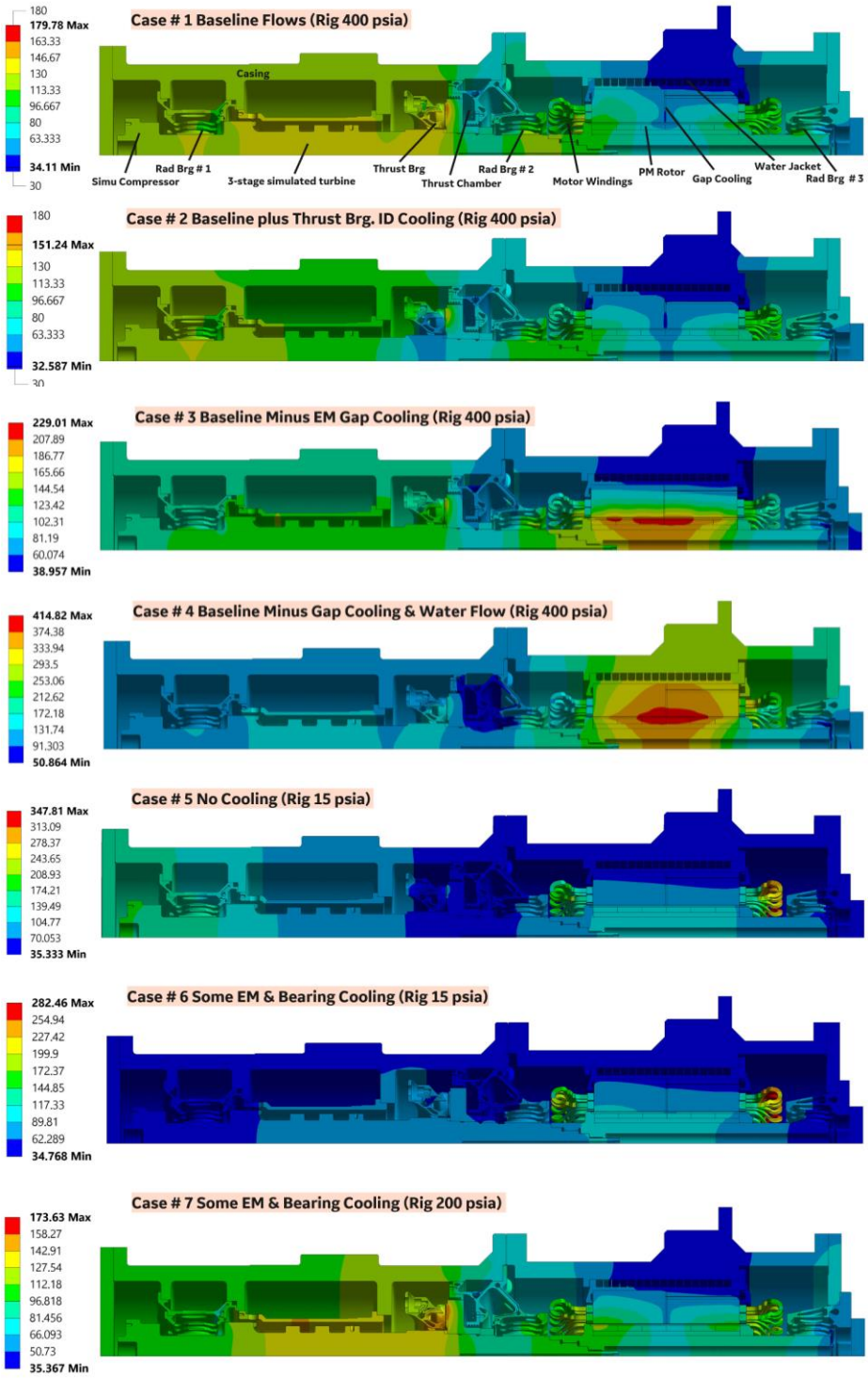

FIGURE 28: Summary of predicted thermal structural temperatures (°C) for the seven cases of Table 1. Some cases have vastly different temperature scales.

For the baseline Case # 1, the overall aerodynamic windage load of the test rig operating at 27krpm was 67.23 kW and the electrical losses in the motor were 6.30 kW, creating a total power load of 73.5 kW for the flow loop. For Case # 1, the thermal model predicted CO_2 exiting the rig in the following state (see Figure 24 for exit locations):

- Rig Exit # 1: 0.34 kg/s CO_2 @ 151.65 ^oC
- Rig Exit # 2: 0.18 kg/s CO_2 @ 89.34 ^oC
- Rig Exit # 3: 0.077 kg/s CO_2 @ 85.6 ^oC

The change in enthalpy of the CO_2 across the rig was about 67.4 kW i.e., majority of the rig heat load is advected out by the CO_2. The water jacket removed 4.16 kW of heat resulting in a water temperature change from 29.44 ^oC at the inlet to 50 ^oC temperature on the exit side, for a water flow rate of 1.4 gpm. The remainder of the heat balance is attributed to natural convection (0.2 kW) from the casing to surrounding air while the rest attributed to numerical round-off errors.

The metal temperatures predicted for the test rig for each of the seven cases of Table 5 are shown in Figure 28. The first four cases presented in Figure 28 correspond to a rig internal pressure of 400 psia (27.6 bara) and have varied levels of CO_2- and water-cooling flows. Gas bearing temperatures are limited based on distortion-induced thin-film clearance closures and damper system performance. The maximum temperatures for the carbon sleeve on the rotor and the stator windings need to be controlled to protect the electrical insulation and prevent failure of the rotating sleeve.

Looking at the baseline case # 1 results, the electric machine temperatures are acceptably below the design threshold. However, the thrust bearing outer radius temperatures are higher than design intent due to the relatively large windage load (large radius, large surface speed) and relatively less cooling. This is remedied in Case # 2, where an additional flow of 0.11 kg/s is introduced between the neighboring pads of the thrust bearing near the inner diameter of the thrust bearing. Comparing Case # 1 and Case # 2 of Figure 28, we see that the overall thrust bearing temperatures are reduced, creating a more ideal operating condition. Note that Case # 1 and Case # 2 results of Figure 28 have identical color scales, so these can be directly compared for the effect of addition of thrust bearing cooling flow. Comparing Case # 1 and Case # 2 results in Figure 28, we see that addition of cooling flow at the thrust bearing cools the test rig in other places due to conduction along the rotor. Addition of cooling flow at the thrust bearing inner diameter, however, creates an undesirable effect of increasing the radial thermal gradient on the pads. This can be seen in Figure 29 where Case # 1 has a thermal differential of about 38^oC between the ID and OD of the pad. Conversely, Case # 2, with a cooler thrust bearing, has a 60 ^oC temperature differential. Thermals loads shown in Figure 28 are used for another FEA model looking at thermomechanical distortions and effects on operating film pressures and gaps in a reference paper [10].

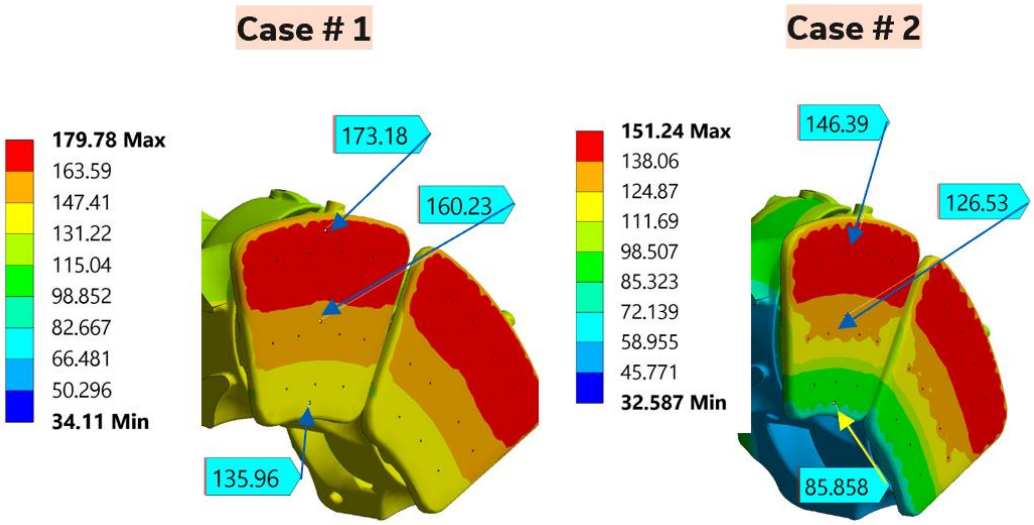

FIGURE 29: Comparison of predicted temperatures on the thrust bearing face for Case 1 and Case 2 of Table 1

In Figure 28, compared to the baseline Case # 1, for Cases # 3 and # 4 (note the different color scales) we see the importance of magnetic gap cooling and the water jacket cooling. Case # 3 shows how removal of the magnetic gap cooling results in high, unacceptable temperatures for the rotor carbon sleeve and permanent magnets. Removal of water cooling further aggravates the issue in Case # 4. We can also see this dramatic change in the cross-section view shown in Figure 30. In Figure 30, we show how the stator windings, the carbon sleeve, the permanent magnets and the stator laminates remain under the desired temperature limits for Case # 1 only. With removal of the magnetic gap cooling flow and further removal of water jacket flow results in unacceptable operating temperatures for the electric machine.

Note that water jacket cooling is a standard method for cooling electric machines [14] and the illustration of Case # 4 is a fairly obvious result. However, a non-obvious and interesting result is seen for Case # 3. The operation of the electric machine at a high-pressure of 400 psia (27.6 bar), 27 krpm results in a windage load of about 7.8 kW locally on the cylindrical surface of the electric machine (comparable to the 6.3 kW of electric loss). Hypothetically, if this electric machine were to operate in CO_2 at atmospheric pressure conditions (instead of 400 psia), the windage load would be one order of magnitude smaller. This is shown for the results of Case # 5 and Case # 6 in Figure 28, where the rig operating pressure is 15 psia. The windage is lower and overall rig temperatures are lower with zero and some EM gap cooling respectively for Case # 5 and Case # 6. Specifically, Case # 5 with an order of magnitude lower electric machine windage (due to low 15 psia rig operation) and zero EM gap cooling leads to acceptable temperatures on the cylindrical surface of the electric machine (i.e., the carbon sleeve and permanent magnets). Note that the stator winding temperature is still high for Case # 5 (max temperature 348 ^{o}C), which is lowered in Case # 6 with the addition of some EM gap cooling and some gas bearing cooling. Thermal results are also presented for Case # 7 (rig operating with intermediate pressure of 200 psia), which shows acceptable thermal results with the addition of some cooling.

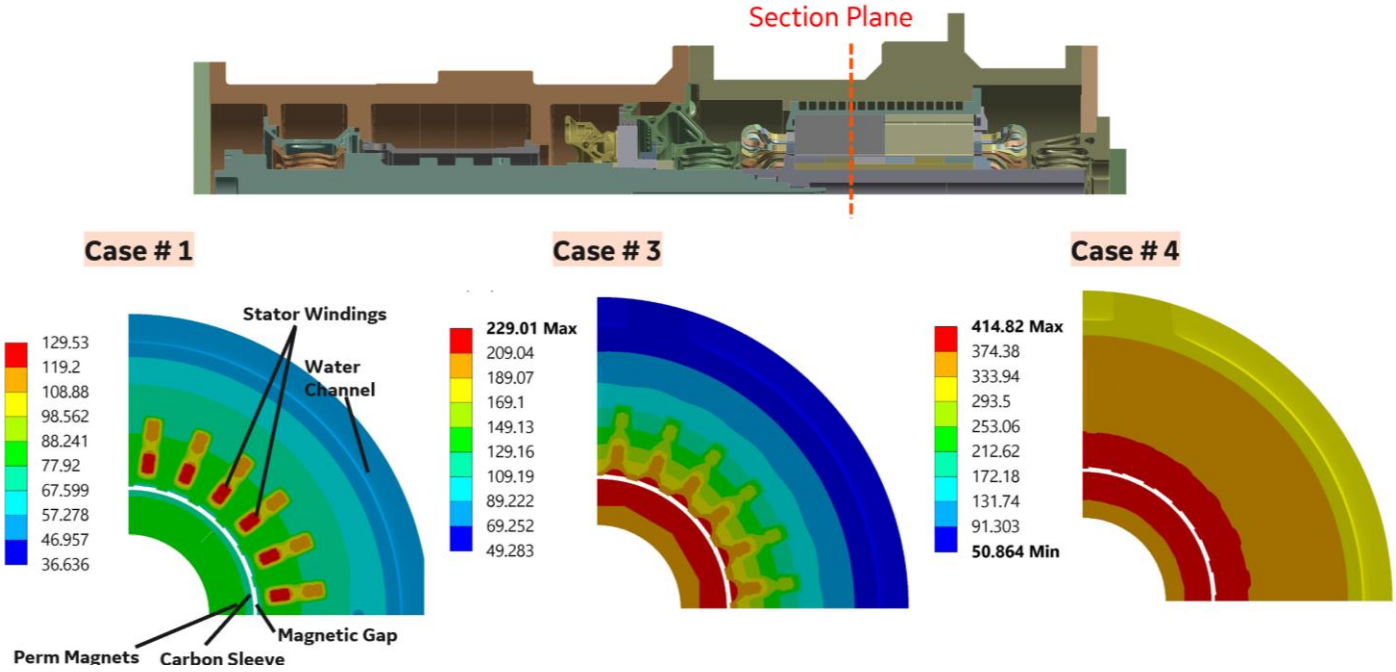

FIGURE 30 Cross-section temperature distribution in the electric machine stator for Cases 1, 3 and 4.

Thus, on account of high-pressure operation, a large amount of heat is generated in the magnetic gap, and it needs to be dissipated by addressing it with the method of magnetic gap cooling [55]. As shown in Figure 29 and Figure 30, the magnetic gap cooling method does work in removing heat successfully and enabling the electric machine operation. As mentioned earlier, similar approach has been reported in the work of Miller et al. [51]. An interesting difference though lies between the size of the cooling port shown in the work of Miller et al. [51] versus the magnetic cooling conduit in this report. The electric machine stator is formed by gluing together several laminates of 0.100-inch thickness as shown in Figure 31. As shown, one of the axially center laminates is modified to create four 90-deg apart radial flow paths that are fed by respective axially drilled holes. The cooling flow path from fluid node 27 to node 35 to node 19 shows the L-shaped travel path for the gap cooling flow. Since the motor stator is minimally disrupted with this approach, our approach results in a compact, power-dense electric machine where the stator doesn't have to be split into two or be interrupted to make space available for the flow ports.

In Figure 32, we show the predicted gas temperatures in the magnetic gap for fluid nodes 15 through 24 (see Figure 24) axially along the cylindrical portion of the electric machine. The fluid node temperature is around 50 ^{o}C at the center and grows to 100 ^{o}C almost symmetrically away from the magnetic gap cooling conduit. Multiple axial locations might need to be introduced for the cooling conduit, if a more uniform axial gas temperature profile is needed.

Finally, in Figure 33, we show how the cooling flow requirements change for the test rig as the internal rig pressure is increased from 15 psia (low-pressure case), 200 psia (intermediate pressure case) and 400 psia (design intent operating point). In Figure 33, the blue circles show the total CO_2 flow going through the rig for each of the seven cases, while the orange circles show the maximum metal temperature predicted in the rig. Interestingly, the maximum

metal temperatures for the baseline Case # 1 (400 psia) and Case # 7 (200 psia) are very comparable. This allows us to directly compare the total CO_2 flow needed for Case # 1 with that of Case # 7 and gain insight into how the cooling flow requirements (kg/s) scale up with internal rig pressure with keeping the maximum rig metal temperature the same. At the same internal rig pressure (comparing Case # 1, 2, 3), we see that more CO_2 flow results in lower maximum rig metal temperatures. Finally, the predicted CO_2 flows for Cases # 5 and # 6 would need to be increased to bring the maximum metal temperatures for those cases in line with Case # 1 and Case # 7. The graph depicted in Figure 33 can be extended to any particular metal temperature node (for e.g., the outer thrust bearing temperature, or the electric machine rotor etc.) to derive similar understanding of metal temperature and cooling flow as function of the rig internal pressures.

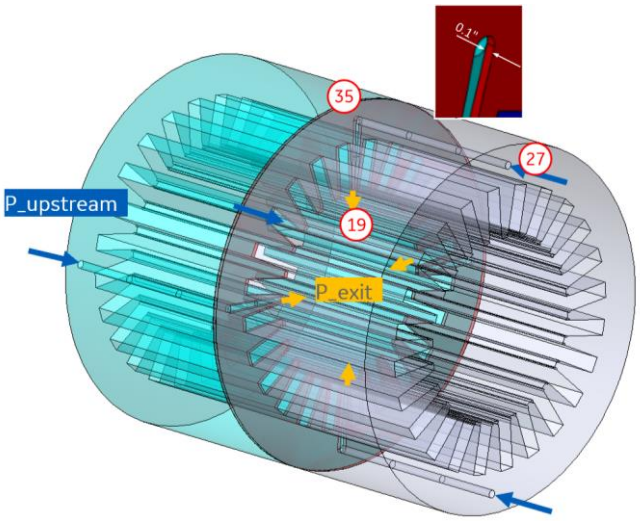

FIGURE 31: 3D path of magnetic gap flow conduit formed by modifying a single 0.100-inch laminate

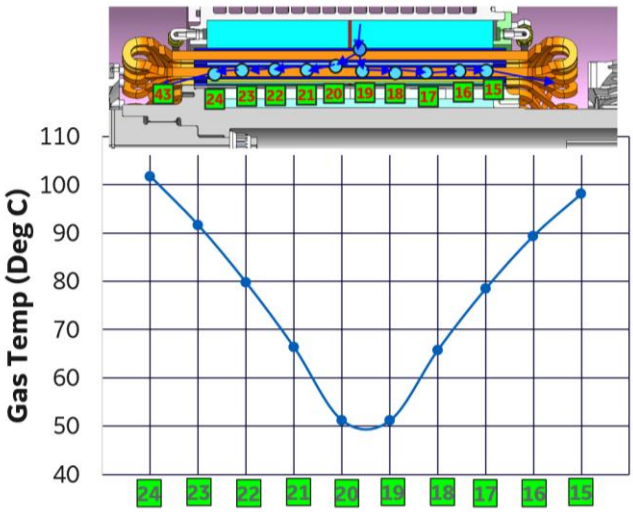

FIGURE 32: Axial distribution of the gas temperature for the 10 fluid nodes of the electric machine magnetic gap

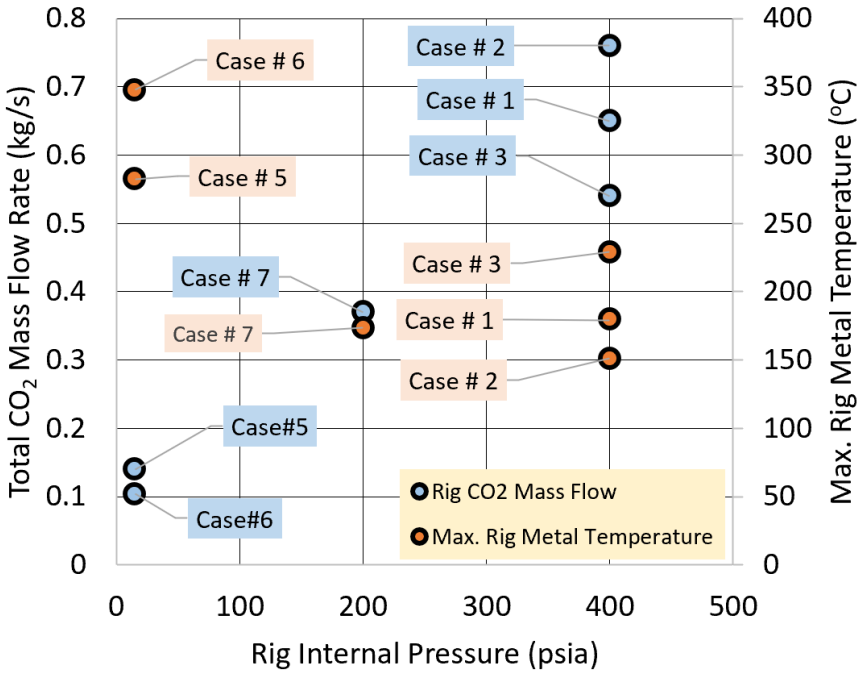

FIGURE 33: Dependence of cooling flow on rig internal operating pressure

11. PROJECT STATUS: HARDWARE FABRICATION, EQUIPMENT PROCURMENT, TESTING

This final section addresses the progress and state of the DOE project. The effort in general can be divided into three main sections: (1) design, (2) hardware fabrication and equipment procurement, and (3) test rig construction and testing. Unfortunately, the program faced funding pressure as well as schedule challenges that necessitated a no-cost-extension in addition to additional funding for reaching program goals.

The design of the test system has been described in detail contained in Section 1-10. For the hardware fabrication Figures 34 and 35 illustrate the state of hardware fabrication. Figure 34 represents all additively manufactured components for this test rig and shows that 3 out of 6 components are completed and the remaining 3 components require minor operations making them 95% complete. Figure 35 shows the remainder of the hardware for fabrication and shows a 100% completion of all major hardware ready for construction.

Figure 36 shows the two major pieces of equipment that are procured and installed in the test cell. The gas supply skid and the VFD for the motor are installed and ready for use once test rig installation is completed.

Figure 37 shows the funding needed to complete execution of program objectives at $577K and Figure 38 shows the schedule and milestones.

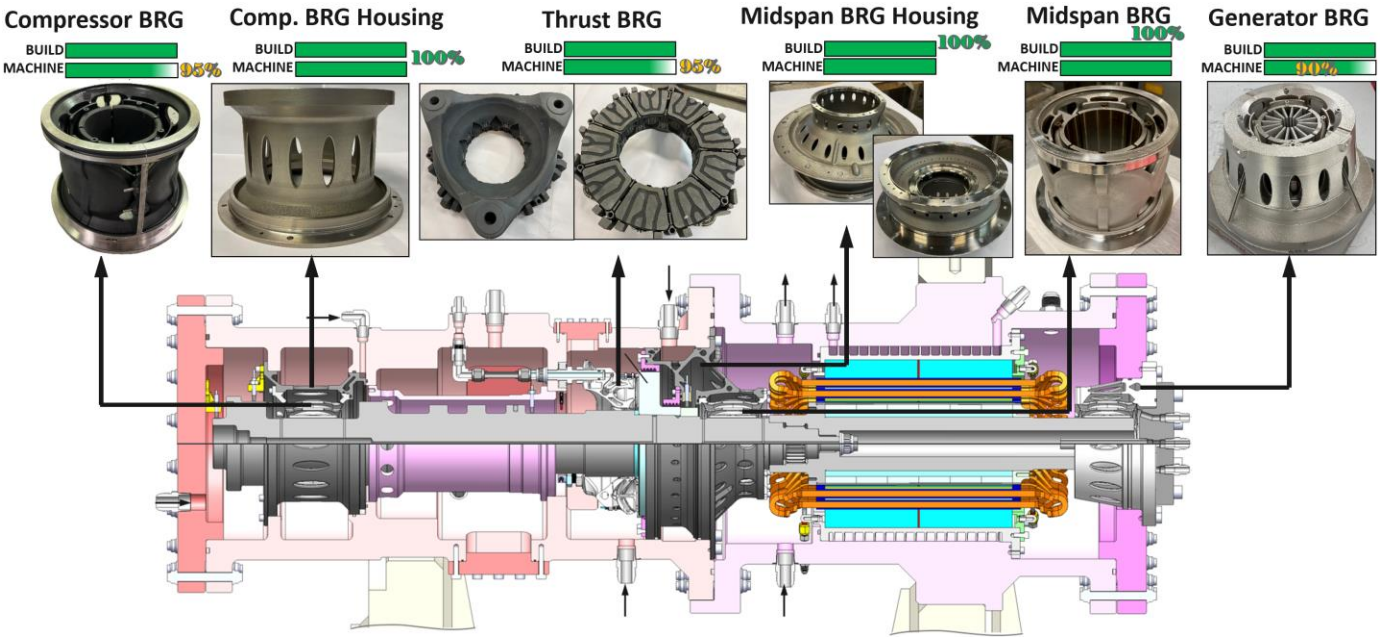

FIGURE 34: Additively manufactured hardware status

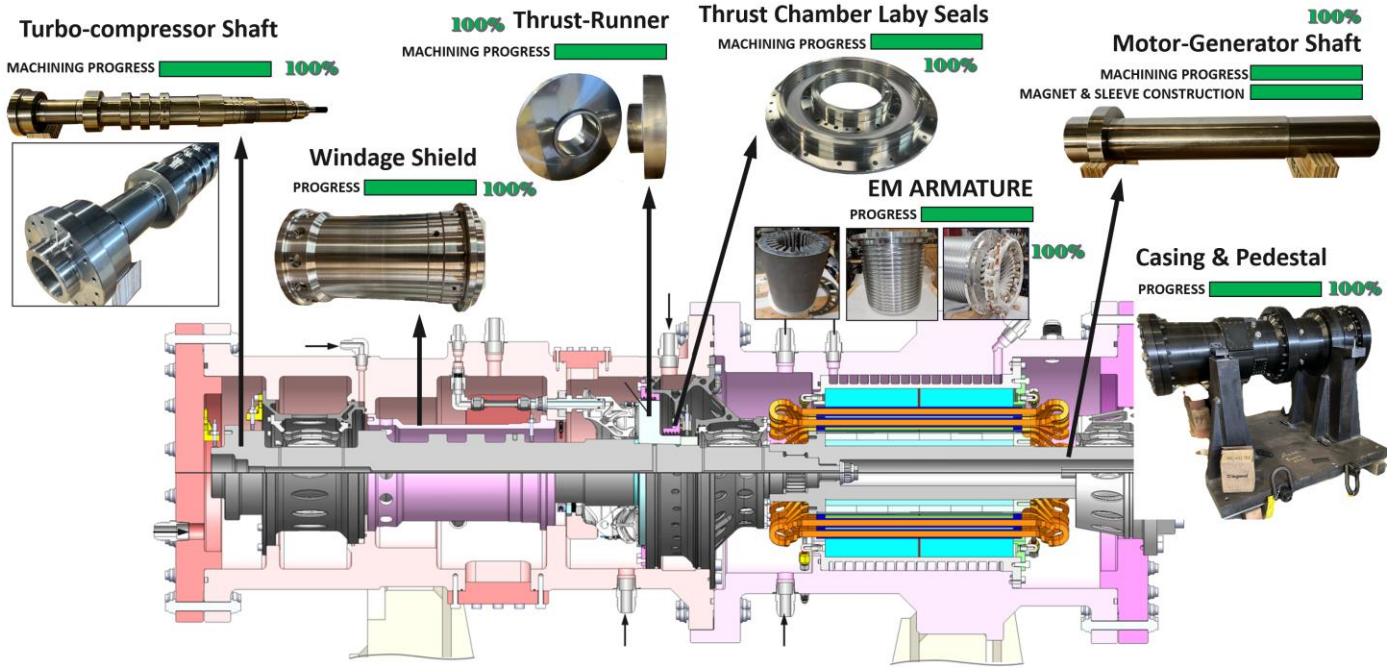

FIGURE 35: All other hardware fabrication status

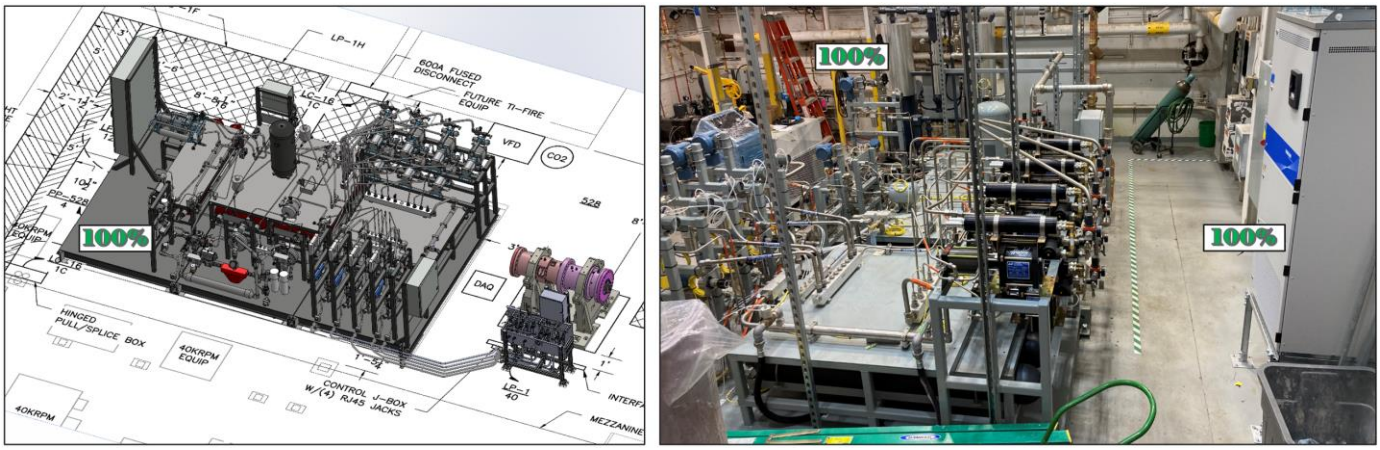

FIGURE 36. Installed equipment, gas supply skid and motor VFD

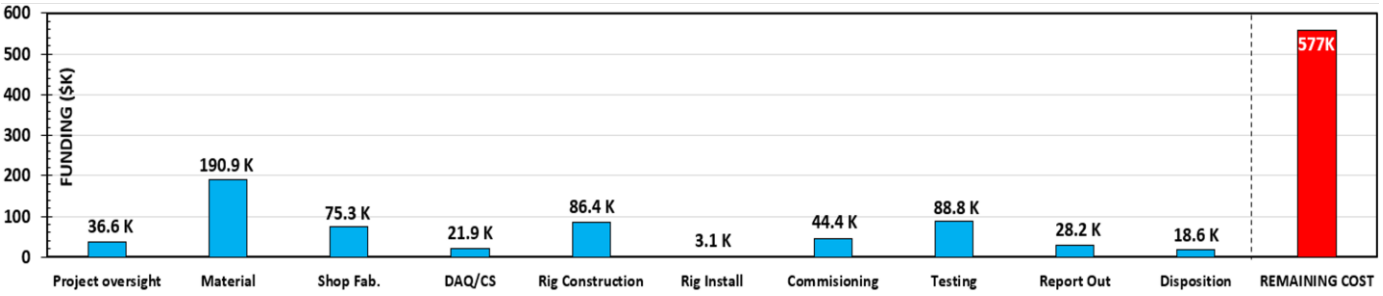

FIGURE 37. Remaining costs for project objective completion

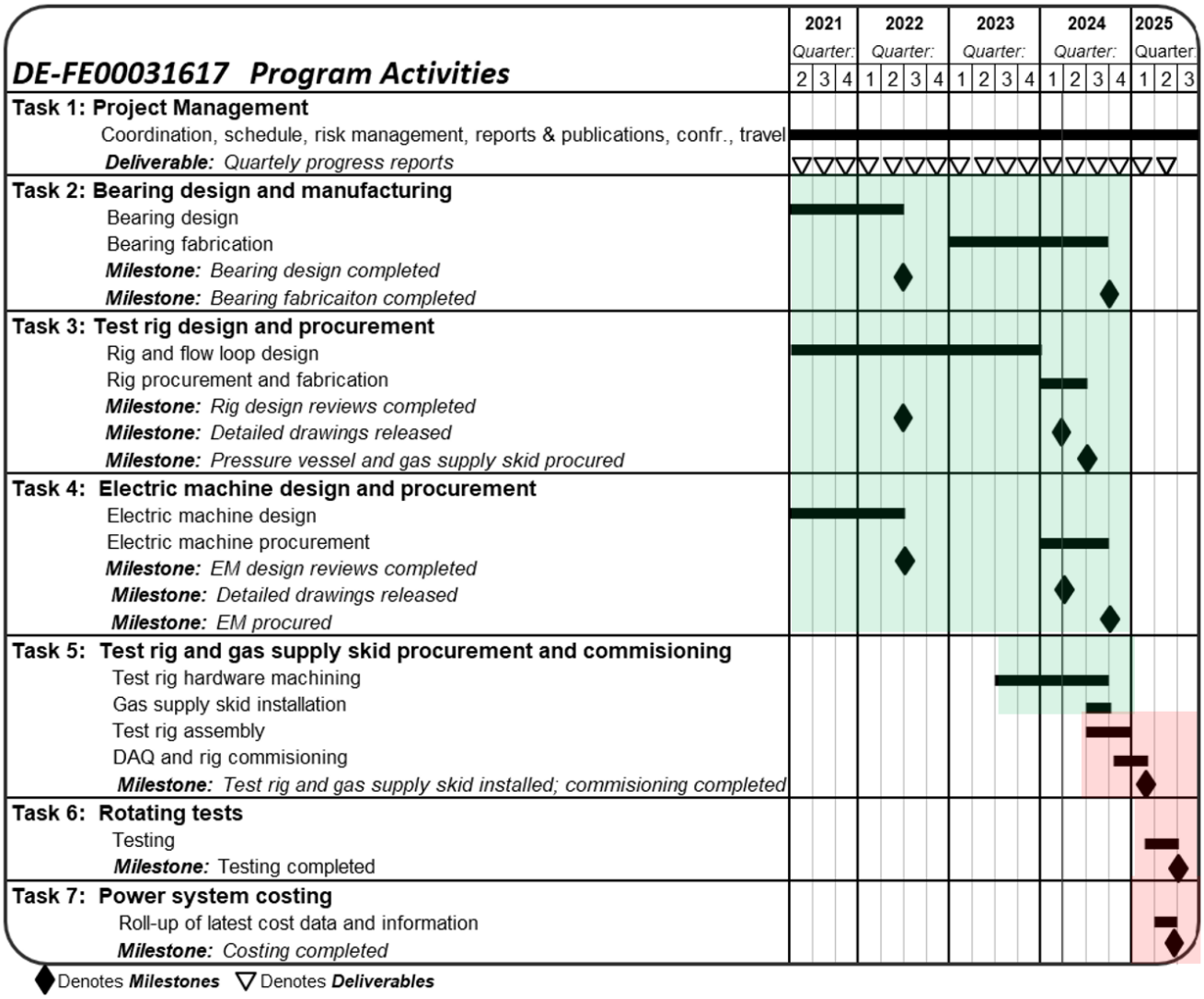

FIGURE 38. Schedule and Milestones

12. CONCLUSIONS

This work described the design and analysis of a custom rotating test rig for reducing technical risks associated with an oil-free hermetic sCO_2 turbomachine. The test rig was design to operate a 180-lbs (82 kg) 53-inch (1.35 m) long three-bearing rotor system to 27-krpm in a 400-psi (27.6-Bar) CO_2 environment. To reduce relevant risks, the test platform was designed to apply thrust, measure thrust, apply rotating unbalance, vary cooling flow schemes, measure operating gas film gaps, monitor rotordynamic vibration, and validate thermal models. An electric machine design was proposed for the test rig and showed to retain the critical operating metrics for reducing risk on the concept such as magnetic gap windage magnitudes and core losses. Novel additively manufactured CO_2 lubricated radial bearings, thrust bearing, and support frames/housings were designed, and critical analysis elements were highlighted. Additionally, additive build trials were performed on the components and showed acceptable manufacturing quality and dimensional control.

The project was shown to be 2/3 complete, as the construction and test phase for the test rig remain. Hardware and equipment are ready to move to the next step for testing if further funding support is granted.

13. REFERENCES

[1] Ma, Z, and Turchi, C, "Advanced Supercritical Carbon Dioxide Power Cycle Configurations for Use in Concentrating Solar Power Systems," NREL/CP-5500-50787, 2011.

[2] Kalra, C. J., Hofer, D., Sevincer, E., Moore, J., and Brun, K., 2014, "Development of High Efficiency Hot Gas Turbo-expander for Optimized CSP Supercritical CO2 Power Block Operation," The Fourth International Symposium—Supercritical CO2 Power Cycles (sCO_2), Pittsburgh, PA, Sept. 9–10, pp. 1–11.

[3] Ancona, A., Bianchi, M., Branchini, L., De Pascale, A., Melino, F., Peretto, A., Torricelli, N., 2021," A Comparison Between Organic Rankine Cycle and Supercritical CO_2 Bottoming Cycles for Energy Recovery from Industrial Gas Turbine Exhaust Gas", ASME J. Eng. Gas Turb. Power, (143) December, 121014-1/11.

[4] Baglietto, G., Maccarini, S., Traverso, A., Bruttini, P., 2022, "Techno-Economic Comparison of Supercritical CO2, Steam, and ORC Cycles for WHR Applications", ASME J. Eng. Gas Turb. Power, GTP-22-1439.

[5] Ghilardi, A., Frate, G. F., Baccioli, A., Ulivieri, D., Ferrari, L., Desideri, U., Cosi, L., Amidei, S., Michelassi, V., 2022, "Techno-Economic Comparison of Several Technologies for Waste Heat Recovery of Gas Turbine Exhausts", ASME J. Eng. Gas Turb. Power, GTP-22-1467.

[6] "Annual Energy Outlook 2022 with projections to 2050." U.S. Energy Information Administration, Washington, DC (2022).

[7] Ertas, B., Zierer, J., McClung, A., Torrey, D., Bidkar, R., Hofer, D., Rallabandi, V., Singh, R., Zhang, X., "Super-Critical Carbon Dioxide Power Cycle for Waste Heat Recovery Utilizing Hermetic Oil-Free Turbomachinery: Cycle and Conceptual Turbomachinery Design", Proceedings of the ASME TurboExpo 2022, GT2023-104245, Boston, MA, June 26-30, 2023.

[8] Hedman, B., "Waste Heat Recovery Opportunities for Interstate Natural Gas Pipelines." Interstate Natural Gas Association of America, Washington DC (2008).

[9] Ertas, B., Hofer, D., April 20, 2021, "Closed-Cycle Heat Engine," U.S. Patent No. 10982713.

[10] Moore, J. J., Cich, S., Day-Towler, M., Hofer, D., Mortzheim, J., "Testing of a 10Mwe Supercritical CO_2 Turbine", Proceedings of the 47th Turbomachinery and 34th Pump Symposia, Houston, TX, September 17-20, 2018.

[11] Mortzheim, J., Hofer, D., Priebe, S., McClung, A., Moore, J. J., Cich, S., "Challenges with Measuring Supercritical CO_2 Compressor Performance When Approaching the Liquid-Vapor Dome", Proceedings of the ASME TurboExpo 2021, GT2021-59527, Virtual Conference, June 7-11, 2021.

[12] Wilkes, J., Wygant, K., Robinson, K., Pelton, R., Bygrave, J., "Design and Testing of a 275 Bar 700 Degree Celsius Expander for an Integrally geared Supercritical CO_2 Compander", Proceedings of the ASME TurboExpo 2022, GT2022-83284, Rotterdam, Netherlands, June 13-17, 2022.

[13] Kleynhans, G., Pfrem, G., Berger, H., Baudelocque, L., "Hermetically Sealed Oil-Free Turbocompressor Technology", Proceedings of the 34th Turbomachinery Symposium, Houston, TX, 2005.

[14] Alban, T., Pellerin, O., Laboube, P., Quoix, B., Gelin, A., Oliva, M., "Mechanical and Performance Testing Method of an Integrated High-Speed Motor Compressor", Proceedings of the 38th Turbomachinery Symposium, Houston, TX, pp. 27-40, 2009.

[15] Buse, M., Van Aarsen, M., Al-Khateeb, E., Al-Jughaiman, B., "Adapting Hermetically Sealed Compressor Technology to Deal With Sour and Corrosive Gases", Proceedings of the 45th Turbomachinery and 32nd Pump Symposium, Houston, TX, September 12-15, 2009.
[16] Conboy, T., Wright, S., Pasch, J., Fleming, D., Rochau, G., Fuller, R., 2012," Performance Characteristics of an Operating Supercritical CO_2 Brayton Cycle", ASME J. Eng. Gas Turb. Power, (134) November, 111703-1/12.
[17] Walker, M. S., Fleming, D. D., Pasch, J. J., "Gas Foil Bearing Coating Behavior in Environments Relevant to S-CO2 Power System Turbomachinery", Proceedings of the 6th International Supercritical CO_2 Power Cycles Symposium, Pittsburgh, PA, March 27-29, 2018.
[18] Ertas, B., and Delgado, A., 2018, "Hermetically Sealed Squeeze Film Damper for Operation in Oil-Free Environments," ASME J. Eng. Gas Turbines Power, 141(2), p. 022503.
[19] Delgado, A., Ertas, B.,2019, "Dynamic Characterization of a Novel Externally Pressurized Compliantly Damper Gas Lubricated Bearing with Hermetically Sealed Squeeze Film Damper Modules," ASME J. Eng. Gas Turbines Power, 141, p. 021028.
[20] Ertas, B. H., 2019, "Compliant Hybrid Gas Bearing Using Integral Hermetically Sealed Squeeze Film Dampers," ASME J. Eng. Gas Turbines Power, 141(10), p. 101020.
[21] Gary, K., Ertas, B. H., 2019, "Experimental Rotordynamic Force Coefficients for a Diffusion Bonded Compliant Hybrid Journal Gas Bearing Utilizing Fluid-Filled Hermetic Dampers," ASME J. Eng. Gas Turbines Power, 142(4), p. 041008.
[22] Ertas, B. H., 2020, "Additively Manufactured Compliant Hybrid Gas Thrust Bearing for sCO_2 Turbomachinery: Design and Proof of Concept Testing," Proceedings of ASME Turbo Expo 2020: Turbomachinery Technical Conference and Exposition IGTI GT2020, Sept., Virtual Conference, ASME Paper 14959.
[23] Miller, J. D., Held, T. J., Sedlacko, K., Hubach, J., Zullo, R., "Test Results of a 1.5MW High Speed Motor-Generator in a Pressurized CO_2 Enviornment," The Sixth International Symposium—Supercritical CO2 Power Cycles (sCO_2), Pittsburgh, PA, March 27-29, 2018.
[24] Bidkar, R., Kumar, U., Zhang, X., Sarawate, N., Powers, J., Anandika, N., Ertas, B., "Test Rig for Evaluating the Performance of a CO_2 Immersed Electro-Mechanical Rotor System Utilizing Gas Bearing: Part-2 Thermal Systems and Flow Loop Design", Proceedings of the ASME TurboExpo 2022, GT2023-103989, Boston, MA, June 26-30, 2023.
[25] Wilkes, J., Cater, R., Swanson, E., Passmore, K., Brady, J., 2018, "The Influence of Ambient Pressure on the Measured Load Capacity of Bump-Foil and Spiral Groove Gas Thrust Bearings at Ambient Pressures up to 69 Bar on a Novel High-Pressure Gas Bearing Test Rig," ASME J. Eng. Gas Turbines Power, 144, p. 061003.
[26] Magge, N., 1975, "Philosophy, Design, and Evaluation of Soft-Mounted Engine Rotor Systems," J. Aircr., 12(4), pp. 318–324.

[27] Memmott, E. A., 1992, “Stability of Centrifugal Compressors by Applications of Tilt Pad Seals, Damper Bearings, and Shunt Holes,” IMechE 5th International Conference on Vibrations in Rotating Machinery, Bath, UK, Sept. 7–10, pp. 99–106.
[28] Memmott, E. A., 2010, “Application of Squeeze-Film Dampers to Centrifugal Compressors,” 28th Machinery Dynamics Seminar (CMVA2010), Ville, QC, Canada, Oct. 27–29, Paper No. CMVA2010-15, pp. 115–129.
[29] Leader, M. E., Whalen, J. K., and Grey, G. G., 1995, “The Design and Application of a Squeeze Film Damper Bearing to a Flexible Steam Turbine Rotor,” 24th Turbomachinery Symposium, College Station, TX, pp. 49–58.
[30] Edney, S. L., and Nicholas, J. C., 1999, “Retrofitting a Large Steam Turbine with a Mechanically Centered Squeeze Film Damper,” 27th Turbomachinery Symposium, Houston, TX, pp. 29–40.
[31] Kanki, H., Kaenko, Y., Kurosawa, M., and Yamamoto, T., 1998, “Prevention of Low-Frequency Vibration of High-Capacity Steam Turbine Units by Squeeze Film Damper,” ASME J. Eng. Gas Turbines Power, 120(2), pp. 391–396
[32] Ertas, B., Cerny, V., Kim, J., and Polreich, V., 2015, “Stabilizing a 46 MW Multistage Steam Turbine Using Integral Squeeze Film Bearing Support Dampers,” ASME J. Eng. Gas Turbines Power, 137(5), p. 052506.
[33] Ferraro, R., Cantanzaro, M., Kim, J., Massini, M., Betti, D., Livermore-Hardy, R., “Suppression of Subsynchronous Vibrations in a 11MW Steam Turbine Using Integral Squeeze Film Dampers”, Proceedings of the ASME TurboExpo 2016, GT2016-57410, Seoul, Korea, June 13-17, 2016.
[34] Zeidan, F. Y., Andres, L. S., and Vance, J. M., 1996, “Design and Application of Squeeze Film Dampers in Rotating Machinery,” 25th Turbomachinery Symposium, Houston, TX, Sept. 17–19, pp. 169–188.
[35] Ertas, B. H., 2021, “Additively Manufactured Compliant Hybrid Gas Thrust Bearing for sCO_2 Turbomachinery: Design and Proof of Concept Testing,” ASME J. Eng. Gas Turbines Power, 143, August, p. 081023.
[36] Ertas, B., Gary, K., Adcock, T., “Identification of Dynamic Force Coefficients for an Additively Manufactured Hermetic Squeeze Film Bearing Support Damper Utilizing a Pass-Through Channel”, Proceedings of the ASME TurboExpo 2023, GT2023-104108, Boston, MA, June 26-30, 2023.
[37] Ertas, B. H., 2020, “Bearing support including hermetic squeeze film damper and accumulator volume”, US Patent No. 10815831.
[38] Ertas, B. H., Gary, K., Delgado, A., 2021, “Additively Manufactured Compliant Hybrid Gas Thrust Bearing for Supercritical Carbon Dioxide Turbomachinery: Experimental Evaluation and Fluid-Structure Model Predictions,” ASME J. Eng. Gas Turbines Power, 143, August, p. 081024.
[39] Delgado, A., Ertas, B. H., 2019, “Dynamic Characterization of a Novel Externally Pressurized Compliantly Damped Gas-Lubricated Bearing with Hermetically Sealed Squeeze Film Damper Modules,” ASME Journal of Engineering for Gas Turbines and Power, 141, February, p. 021028.

[40] American Petroleum Institute, 1996, "Tutorial on the API Standard Paragraphs Covering Rotor Dynamics and Balancing: An Introduction to Lateral Critical and Train Torsional Analysis and Rotor Balancing," Standard Paragraphs API Publication 684, Feb.
[41] "Annual Energy Outlook 2022 with projections to 2050." U.S. Energy Information Administration, Washington, DC (2022).
[42] Ertas, B., Zierer, J., McClung, A., Torrey, D., Bidkar, R., Hofer, D., Rallabandi, V., Singh, R., Zhang, X., "Super-Critical Carbon Dioxide Power Cycle for Waste Heat Recovery Utilizing Hermetic Oil-Free Turbomachinery: Cycle and Conceptual Turbomachinery Design", Proceedings of the ASME TurboExpo 2023, GT2023-104245, Boston, MA, June 26-30, 2023.
[43] Ertas, B. H., 2021, "Additively Manufactured Compliant Hybrid Gas Thrust Bearing for sCO_2 Turbomachinery: Design and Proof of Concept Testing," ASME J. Eng. Gas Turbines Power, 143, August, p. 081023.
[44]. Ertas, B., Gary, K., Adcock, T., "Identification of Dynamic Force Coefficients for an Additively Manufactured Hermetic Squeeze Film Bearing Support Damper Utilizing a Pass-Through Channel", Proceedings of the ASME TurboExpo 2023, GT2023-104108, Boston, MA, June 26-30, 2023.
[45] R. A. Bidkar, E. Sevincer, J. Wang, A. M. Thatte, A. Mann, M. Peter, G. Musgrove, T. Allison and J. Moore, 2017, "Low leakage shaft-end seals for utility-scale supercritical CO_2 turboexpanders," Journal of Engineering for Gas Turbines and Power, Vol. 139(2), 022503.

[46] D. Trivedi, R. A. Bidkar, C. Wolfe and X. Zheng, "Film-stiffness characterization for supercritical CO2 film-riding seals," GT2018-76161, ASME 2016 Turbo Expo, Oslo, Norway, June 11 - 15, 2018

[47] Moore, J. J., Cich, S., Day-Towler, M., Hofer, D., Mortzheim, J., "Testing of a 10MWe Supercritical CO_2 Turbine", Proceedings of the 47th Turbomachinery and 34th Pump Symposia, Houston, TX, September 17-20, 2018.
[48] Mortzheim, J., Hofer, D., Priebe, S., McClung, A., Moore, J. J., Cich, S., "Challenges with Measuring Supercritical CO_2 Compressor Performance When Approaching the Liquid-Vapor Dome", Proceedings of the ASME TurboExpo 2021, GT2021-59527, Virtual Conference, June 7-11, 2021.
[49] Wilkes, J., Wygant, K., Robinson, K., Pelton, R., Bygrave, J., "Design and Testing of a 275 Bar 700 Degree Celsius Expander for an Integrally geared Supercritical CO_2 Compander", Proceedings of the ASME TurboExpo 2022, GT2022-83284, Rotterdam, Netherlands, June 13-17, 2022.
[50] Ertas, B., Powers, J., Gary, K., Torrey, D., Zierer, J., Baehmann, P., Rallabandi, V., Adcock, T., Anandika, N., Bidkar, R., "Test Rig Concept for Evaluating the Performance of a CO_2 Immersed Electro-Mechanical Rotor System Utilizing Gas Bearings: Part-1 Mechanical and Electric Machine Design", Proceedings of the ASME TurboExpo 2023, GT2023-104093, Boston, MA, June 26-30, 2023.
[51] Miller, J., Held, T., Sedlacko, K., Hubach, J., Zullo, R., "Test Results of a 1.5MW High Speed Motor-Generator in a Pressurized CO_2 Environment", Proceedings of the 6th Intl. sCO_2 Power Cycles Symposium, Pittsburgh, PA, March 27-29, 2018.

[52] Alban, T., Pellerin, O., Laboube, P., Quoix, B., Gelin, A., Oliva, M., "Mechanical and Performance Testing Method of an Integrated High-Speed Motor Compressor", Proceedings of the 38th Turbomachinery Symposium, Houston, TX, pp. 27-40, 2009.
[53] Kalra, C. J., Hofer, D., Sevincer, E., Moore, J., and Brun, K., 2014, "Development of High Efficiency Hot Gas Turbo-expander for Optimized CSP Supercritical CO2 Power Block Operation," The Fourth International Symposium—Supercritical CO2 Power Cycles (sCO_2), Pittsburgh, PA, Sept. 9–10, pp. 1–11.
[54] EL-Refaie, A. M., Alexander, J. P., Galioto, S., Reddy, P. B., Huh, K., de Bock, P., and Shen, X., "Advanced High-Power-Density Interior Permanent Magnet Motor for Traction Applications", IEEE Transactions on Industry Applications, 50 (5), 2014, pp 3235-3248.
[55] Ertas, B. H., Zierer, J. J., Torrey, D., Rallabandi, V., Crall, D., Pazinski, A., Mohamed, M., Sibbach, A. W., "Magnetic Gap Cooling Scheme For Permanent Magnet Electric Machines", US Patent Application Serial Number 18/085,962, Dec. 21, 2022.

14. PRODUCTS

Ertas, B.H., Gary, K., Adcock, T., 2023, "Identification of Dynamics Force Coefficients for an Additively Manufactured Hermetic Squeeze Film bearing Support Damper Utilizing a Pass-Through Channel", Proceedings of the ASME TurboExpo 2023, June 26-30, Paper No. GT2023-104108. ***BEST PAPER AWARD***

Ertas, B., Zierer, J., McClung, A., Torrey, D., Bidkar, R., Hofer, D., Rallabandi, V., Singh, R., Zhang, X., 2023 "Super-Critical Carbon Dioxide Power Cycle for Waste Heat Recovery Utilizing Hermetic Oil-Free Turbomachinery: Cycle and Conceptual Turbomachinery Design", Proceedings of the ASME TurboExpo 2023, Boston, MA, June 26-30, Paper No. GT2023-.104245.

Ertas, B., Powers, J., Gary, K., Torrey, D., Zierer, J., Baehmann, P., Rallabandi, V., Adcock, T., Anandika, N., Bidkar, R., 2023 "Test Rig for Evaluating the Performance of a CO_2 Immersed Electro-Mechanical Rotor System Utilizing Gas Bearings: Part-1 Mechanical and Electric Machine Design", Proceedings of the ASME TurboExpo 2023, Boston, MA, June 26-30, Paper No. GT2023-.104093.

Bidkar, R., Kumar, U., Zhang, X., Sarawate, N., Powers, J., Anandika, N., **Ertas, B.**, 2023 "Test Rig for Evaluating the Performance of a CO_2 Immersed Electro-Mechanical Rotor System Utilizing Gas Bearing: Part-2 Thermal Systems and Flow Loop Design", Proceedings of the ASME TurboExpo 2023, Boston, MA, June 26-30, Paper No. GT2023-.1103989.

Ertas, B.H., Gary, K., 2021, "Frequency Dependency of Dynamic Force Coefficients for Hermetic Squeeze Film Dampers Utilizing Fluid-Bounding Flexible Structures", Proc. Gas Turbine Tech. Conf. Exp. ASME Turbo Expo, Virtual Event, June 7-11, Paper No. GT2021-60007. ***BEST PAPER AWARD***